Project No. 11-3004

A High Temperature-tolerant and Radiation-resistant In-core Neutron Sensor for Advanced Reactors

Nuclear Energy Enabling Technology

Dr. Lei Cao
The Ohio State University

Suibel Schuppner, Federal POC
Troy Unruh, Technical POC

NEUP Nuclear Energy University Programs
U.S. Department of Energy

FINAL REPORT

Project title: A High Temperature-tolerant and Radiation-resistant In-core Neutron Sensor for Advanced Reactors

Covering Period: September 11th, 2011 to September 30th, 2014

Date of Report: November 30th, 2014

Recipient: The Ohio State University
201 W 19TH Avenue
Columbus, Ohio 43210

Award Number: DE-AC07-051D14517

Principal Investigator: Lei Cao, 614-247-8701, Cao.152@osu.edu

Co-PI: Don Miller, Miller.68@osu.edu

Project Objective: The objectives of this project are to develop a small and reliable gallium nitride (GaN) neutron sensor that is capable of withstanding high neutron fluence and high temperature, isolating gamma background, and operating in a wide dynamic range. The first objective will be the understanding of the fundamental materials properties and electronic response of a GaN semiconductor materials and device in an environment of high temperature and intense neutron field. To achieve such goal, an in-situ study of electronic properties of GaN device such as I-V, leakage current, and charge collection efficiency (CCE) in high temperature using an external neutron beam will be designed and implemented. We will also perform in-core irradiation of GaN up to the highest yet fast neutron fluence and an off-line performance evaluation.

Table of Contents

1. Executive Summary 3
2. Detector Fabrication and Characterization 4
   2.1 Semi-Insulating Material 4
      2.1.1 Electrical Characteristics 5
      2.1.2 Radiation Response 6
   2.2 Gd:GaN Superlattice Material 7
      2.2.1 Electrical Characteristics 8
      2.2.2 Radiation Response 8
   2.3 Unintentionally Doped Material 9
      2.3.1 Device Fabrication 9
      2.3.2 Maskless Photolithography 12
      2.3.3 High Temperature Optimization 14
      2.3.4 Wafer Dicing 14
      2.3.5 Electrical Characteristics 15
      2.3.6 Radiation Response 21
3. TCAD Simulation 28
      3.1.1 Built-in Electric Field 28
      3.1.2 Impact Ionization, Recombination and Trapping 28
      3.1.3 Collected Charge Deconvolution 32
4. Neutron Detection 34
   4.1 Neutron Detection in High Flux 34
   4.2 Neutron Detection after In-core Irradiation 38
5. Conclusions 42
6. Publication list 43
7. References 44

1. Executive Summary

This report documents the progress in fabrication and characterization of a gallium nitride (GaN) based neutron detector for high temperature operation in high neutron fluence environments. Detectors were fabricated on a variety of GaN materials, including semi-insulating GaN and Gd:GaN superlattice material, with the most successful devices coming from detectors constructed from unintentionally doped n-type GaN. All devices were assessed for their current-voltage (I-V) and radiation response characteristics.

Vertical Schottky diodes fabricated from unintentionally doped n-type GaN were found to be responsive to α-particles, and the charge collection efficiency (CCE) of these devices was found to be between 3-7% at room temperature. The detectors did not exhibit sensitivity to γ-rays or β-particles. Capacitance-voltage measurements were performed on the devices and used to measure the doping levels and depletion depths when reversely biased. Doping levels in the unintentionally doped GaN were found to range between 9.0×10^{15} cm^{-3} and 1.9×10^{16} cm^{-3}, and restricted the depletion region to less than 2 μm.

The radiation resistance of the detectors was characterized with I-V, C-V, and CCE measurements before and after neutron irradiation at different fluences. The I-V and C-V measurements confirmed that the interface state changes at the interfacial layer and that the deep levels induced by neutron irradiation are responsible for the slight change in the I-V characteristics. Both a lower-energy peak shift of the alpha spectra and a slight drop in CCE were observed for the GaN devices after receiving 10^{15} n/cm^2 in-core neutron irradiation. These phenomena were attributed to the electron traps introduced by neutron irradiation. The loss of Schottky contact behavior was observed for fluences above 10^{16} n/cm^2.

Devices were shown to detect neutrons when paired with a ^{6}Li conversion material, and demonstrated evidence of intrinsic detection via neutron capture in ^{14}N. Temperature dependent I-V measurements were also performed to characterize the detectors for high temperature operation. Modeling of the detector leakage current at high temperatures showed leakage current could become prohibitively high at temperatures above 400 ˚C for the chosen material. Neutron detection at high temperature was not achieved due to significant noise issues in the test chamber. However, from the experiments performed, we believe the GaN sensors could detect neutrons at elevated temperatures. The true limitation of GaN based detectors lies in the quality of available material.

2. Detector Fabrication and Characterization

Over the course of this project, several varieties of GaN material were used in the fabrication of radiation detectors. The dislocation density, doping levels, and impurity levels varied considerably between each material, and devices were fabricated on each, with varying degrees of success. The first material used in the fabrication of a GaN devices were bulk, semi-insulating, ~450 µm thick wafers. Gd:GaN superlattice wafers were then fabricated into Schottky barrier detectors, followed by unintentionally doped GaN material.

2.1 Semi-Insulating Material

Devices were initially fabricated from semi-insulating GaN freestanding wafers. Semi-insulating GaN grown using the ammonothermal method was procured from Ammono[1], S. A. The ammonothermal growth method utilizes supercritical NH_3 with a high purity, polycrystalline GaN feedstock in a two zone autoclave. GaN single crystals grown using this method have the lowest dislocation density of any material commercially available, on the order of 10^5 cm^{-2}. Wafers were also purchased from Kyma Inc., which were grown using Hydride Vapor Phase Epitaxy (HVPE), a quicker growth method that has the unfortunate side effect of higher dislocation density (10^6 cm^{-2}).

The semi-insulating wafers from both companies were used to make vertical Schottky diodes for radiation detection. Si-ion implantation was used to dope one side of each wafer to facilitate ohmic contact formation. Ion implantation was performed by an external vendor, Leonard Kroko Inc., using the parameters specified in Table 1.

Table 1. Si-ion Implantation Conditions.

Energy (keV)	50
Fluence (cm^{-2})	1×10^{16}
Temperature (°C)	300
Angle of Incidence (deg)	7

The samples were then placed in a Rapid Thermal Annealer (RTA) for 1 minute at 1150 °C under N_2 gas at atmospheric pressure for activation of the Si dopant. A Ti/Al/Ni/Au (10nm/200nm/20nm/300nm) ohmic contact was then deposited on the Si-doped side of the wafer using electron beam evaporation. Schottky contacts were realized using photolithography with a contact aligner and e-beam evaporation of Ni/Au (20nm/300nm).

[1] Certain commercial products are identified in this reprot in order to specify the experimental procedures in adequate detail. This identification does not imply recommendation or endorsement by the authors, nor does it imply that the products identified are necessarily the best available for the purpose.

2.1.1 Electrical Characteristics

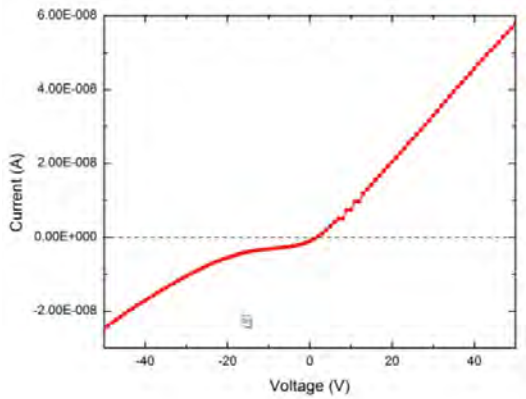

Figure 1. Ammono diode I-V measurement.

I-V measurements in the Ammono sample exhibited slightly rectifying behavior under reverse bias, and relatively low leakage current (10 nm at -30 V)(Figure 1). The low current observed in the device under reverse and forward bias can be attributed to the semi-insulating properties of the material and high resistivity (>10^6 Ω-cm).

I-V measurements in the Kyma semi-insulating GaN showed even lower leakage current than the Ammono material (1.5 nA at -200 V) in 3 of the 4 devices (Figure 2). However, the contacts on the Kyma material resembled ohmic junctions, despite the fact that Schottky diodes were the intended goal.

We opted to use Depth Resolved Cathodoluminescence Spectroscopy (DRCLS), which is an existing resource in our unfunded collaborator (Dr. Leonard Brillson' lab) rather than purchasing new equipment, to investigate the trapping levels within the bandgap of GaN. DRCLS is a technique that allows one to investigate the concentration and energy level of defects in a bulk material, as a function of depth. Results of the DRCLS showed that the Near Band Edge (NBE) emission, the luminescence peak associated with the bandgap of a semiconductor, was completely absent in the Ammono semi-insulating material. This result was attributed to the presence of Mg dopants, used to compensate the natural n-type doping of GaN. However, the high levels of Mg removed the semiconducting properties of the material, making the material an insulator.

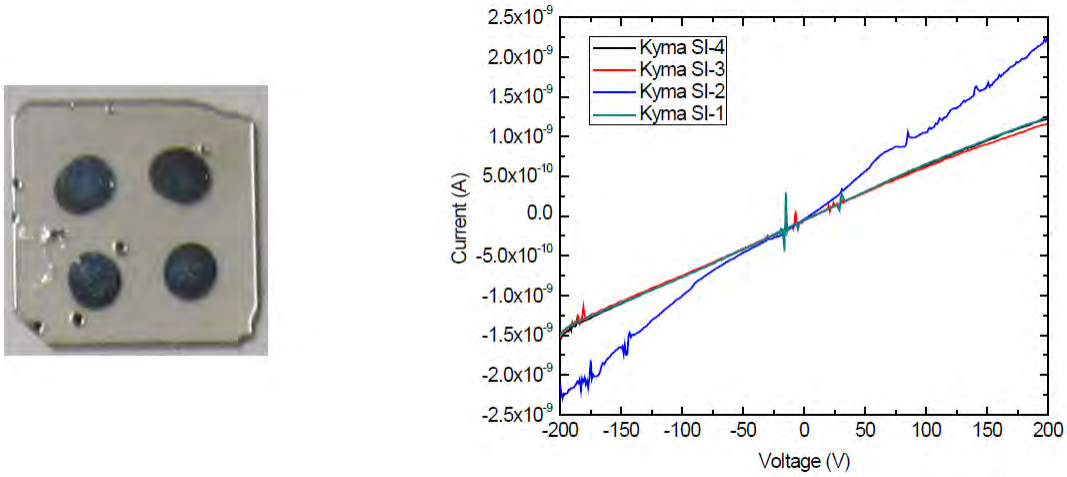

Figure 2. Schottky contacts on semi-insulating Kyma GaN (left) and I-V measurements on 4 devices.

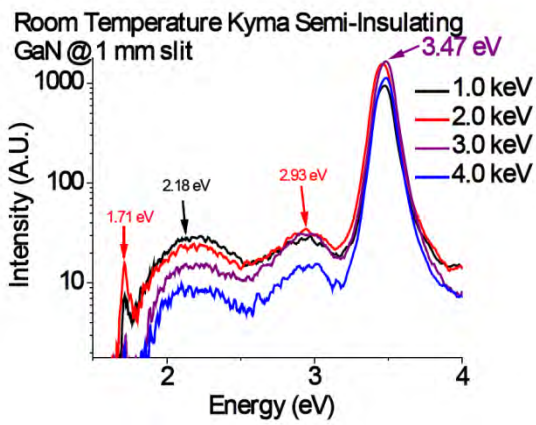

Figure 3. DRCLS for semi-insulating Kyma GaN.

DRCLS measurements on the semi-insulating Kyma material did indicate an intense NBE peak, despite the presence of Fe doping for compensation (Figure 3). Blue (2.93 eV) and yellow (2.18 eV) luminescence was also observed in the Kyma material, likely due to Fe^{2+}/Fe^{3+} energy levels and Ga vacancies (V_{Ga}), respectively. The relative intensities of the BL and YL peaks to the NBE peak decreased with increasing e-beam intensity, indicating that the concentration of Fe doping and V_{Ga} was lower in the bulk material compared to the wafer surface.

2.1.2 Radiation Response

Both the Ammono and Kyma semi-insulating GaN diodes were still tested for spectroscopic response of an ^{241}Am α-particle source. Measurements were taken in vacuum over a range of reverse biases, with pulses analyzed using a 14-bit, 100 MHz CAEN N6724 digitizer, equipped with a trapezoidal filter. Unfortunately, both types of semi-insulating GaN detectors were unable to acquire any pulses from the ^{241}Am source.

Despite having leakage current sufficiently low for detection of pulses, it was determined that the large concentration of compensating dopants (Mg for Ammono and Fe for Kyma) created a high concentration of trapping sites in the detectors. These sites trapped electron-hole pairs generated by alpha particles while drifting to the anode and cathode, resulting in no pulses collected in the preamplifier.

2.2 Gd:GaN Superlattice Material

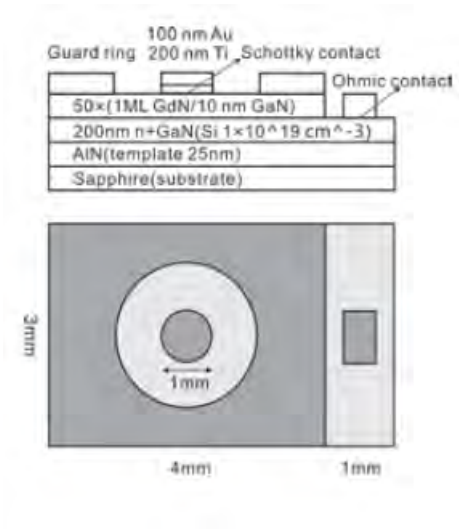

Figure 4. Plan and cross-section view of Gd:GaN superlattice detector.

Devices were also fabricated using superlattice Gd:GaN material, provided by unfunded collaborator Dr. Roberto Myer at the Department of Materials Science and Engineering at OSU. Incorporating Gadolinium into the device is desirable as the thermal neutron capture cross section for natural Gd is 49,000 b. The material was grown using Molecular Beam Epitaxy (MBE) to form a 10 nm layer of undoped GaN and 2.4 monolayers of Gd. This layering was repeated 50 times, giving a ≈650 nm thick superlattice of Gd:GaN. A 25 nm AlN layer and highly doped GaN buffer layer were grown below the supper lattice to ease stress due to lattice mismatch between the substrate (sapphire) and GaN, and to provide a conductive layer for ohmic contact deposition (Figure 4).

Detectors were fabricated by first masking the majority of the wafer with photoresist, and etching a section of the exposed superlattice with an Inductively Coupled Plasma-Reactive Ion Etcher (ICP-RIE). After stripping the protective photoresist, the wafer's etched depth was measured using a Sloan Dektak3 Profilometer to determine how much material was removed during the etching process. This process was repeated several times to empirically determine the etch rate of the superlattice (Figure 5).

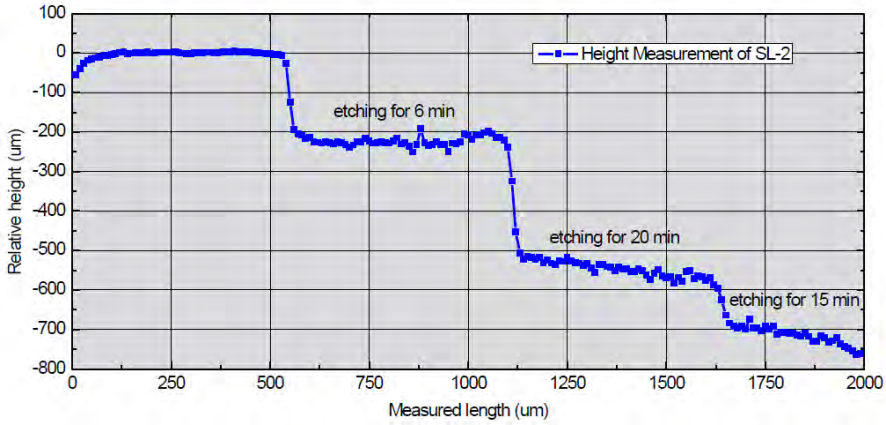

Figure 5. Superlattice wafer profile after several rounds of ICP-RIE.

Once establishing the etch rate to be 17 nm/min with 20 sccm Cl_2, 5 sccm Ar, 40 Watts RIE power, and no ICP, the material was etched down to the highly doped buffer layer. A Ti/Al/Ni/Au contact was deposited on the n+ GaN buffer layer using standard photolithography techniques and e-beam evaporation. Schottky Ni/Au contacts were deposited on the Gd:GaN superlattice in a similar manner.

2.2.1 Electrical Characteristics

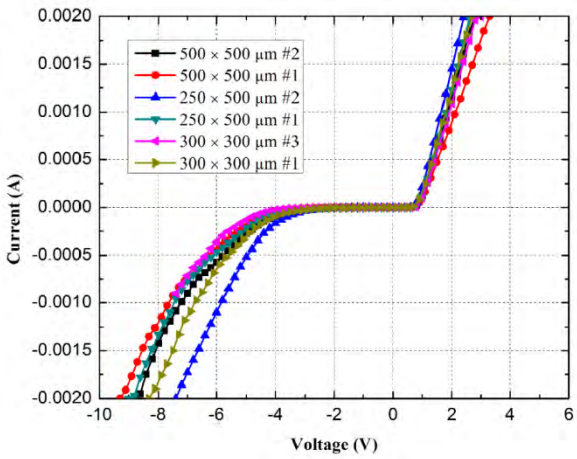

Figure 6. I-V measurements of superlattice Gd:GaN detectors.

I-V measurements were performed on several of the superlattice Schottky diodes to determine the detectors' reverse bias characteristics. Results of these measurements (Figure 6) showed all of the detectors had leakage current above what would be considered optimal for use in radiation detection. The high leakage current was attributed to the increased carrier concentration from the Gd material.

2.2.2 Radiation Response

Detectors fabricated from the Gd:GaN superlattice material were used to obtain the

alpha spectrum from ^{241}Am, using the same experimental setup from characterizing the semi-insulating GaN detectors. Once again, the detectors failed to show a response to the alpha particles. One reason for the lack of response was attributed to the very thin (650 nm) active detector region. In such a thin detector, only 100 keV of the alpha particle's energy would be deposited in the active region, which is far too small to distinguish from the high leakage current in the detector. Additionally, the interface between Gd and GaN layers could form potential barriers, hampering the transportation of charge carriers generated in the detector.

2.3 Unintentionally Doped Material

Following the unsuccessful attempts to fabricate a radiation detector on superlattice GaN, unintentionally doped material was procured from Kyma, Inc. This material, like the semi-insulating GaN, was grown via HVPE to create freestanding, ≈450 µm thick wafers. Although this material has a relatively high dislocation density (5×10^6 cm^{-2}), it was believed that this material could work due to its lack of dopants which prevented signal collection in previous devices. While there are no dopants intentionally added during growth, grown GaN is consistently n-type. The wide bandgap of GaN (3.4 eV) prohibits the production of thermally generated carriers, and its n-type characteristics must therefore be from an impurity or defect related donor. Studies have shown [1] that defects which form during growth (V_N, V_{Ga}, V_{Ga}- V_N) or impurities (C, O) create excess charge carriers, leaving the material n-type. Although the unintentional doping level in this material can be quite high (10^{16} cm^{-3}), work proceeded towards fabricating a radiation detector. Wurtzite, C-plane, freestanding, 1 cm × 1 cm wafers with an epi-ready Ga-face and optical polish N-face were procured for processing.

2.3.1 Device Fabrication

Fabrication of detectors on unintentionally doped GaN was quite similar to the procedure used on the semi-insulating material. Removal of organics from the wafer was accomplished with a 2 minute ultrasonic bath in acetone, then isopropyl alcohol (IPA), followed by a deionized water rinse and 1 minute of N_2 drying. Shipley 1813 photoresist was spin coated over the Ga-surface of the wafer to protect the epi-ready surface during ohmic contact deposition on the backside N-surface. The photoresist was flood exposed for 6 seconds under i-line, 365 nm UV light, using an EV 620 contact aligner, to allow for easier resist removal following ohmic contact deposition. A 30 sec dip in HF:DI (1:10) performed to remove any native oxide on the backside of the wafer, followed by promptly loading the wafer into the e-beam evaporator to minimize oxide regrowth.

Metal deposition in the CHA Solutions E-Gun Evaporator proceeded once the pressure in the chamber reached 2×10^{-6} Torr. The metallization of the N-face consisted of a Ti/Al/Ni/Au (10nm/200nm/20nm/300nm) stack. Following metal deposition, the wafer was stripped of photoresist using n-methyl-2-pyrrolidinone (NMP) for 5 minutes, and placed in an oxygen plasma "asher" for 15 minutes operating at 45 W, 13.56 MHz RF, with 25 sccm

oxygen flow to remove any residual resist that could be permanently baked on to the surface during rapid thermal annealing (RTA). Annealing of the ohmic contact was subsequently performed in an AGA 410 RTA, heating the wafer to 750°C for 30 s, under a 20 sccm N_2 flow. While the relatively high doping levels in the GaN wafer preclude the need for Si implantation to form a good ohmic contact, annealing the wafer increasing the doping level just below the contact by forming TiN complexes, essentially increasing the concentration of V_N. The 300 nm Au cap is used to prevent oxidation in the ohmic contact during annealing and high temperature operation. While this was the intended purpose of the Au layer, visual inspection of the wafer post-anneal showed some oxidation (Figure 7), although this oxidation did not appear to affect the performance of the device.

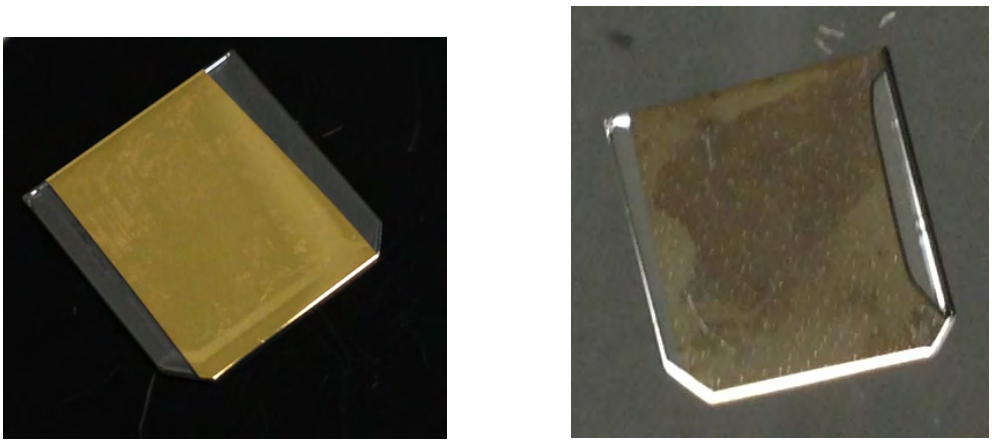

Figure 7. Backside ohmic contact before and after rapid thermal annealing.

Schottky barrier realization was performed by cleaning the wafer again with acetone and IPA, and spin coating with Lift Off Resist (LOR) 5A and S1813 photoresist. 1 mm circular pads with 0.4 mm thick concentric guard rings, spaced 0.1 mm from the periphery of the pads were patterned on the wafer using a contact aligner and custom photomask (Figure 8).

Photoresist was developed in MF-319 for 2 minutes, rinsed with DI water, and dried with N_2. The wafer was then placed in an HF:DI (1:10) dip for 30 seconds, an O_2 plasma asher for 15 minutes, and immediately into the e-beam evaporator. Ni/Au (20nm/300nm) layers were deposited on the Ga-face of the wafer once the pressure dropped below 2×10^{-6} Torr, and subsequently placed in NMP at 85˚C for 15 minutes. The wafer and NMP solution were then placed in an ultrasonic bath for 1 minute, followed by an IPA rinse, and finally a DI water rinse with N_2 dry.

Figure 8. 5-inch, chrome plated, soda lime photomask for device patterning in photoresist.

I-V measurements were performed with a probe station to determine which diodes were successfully fabricated, reducing the number of detectors to be wire bonded. The wafer was then mounted in a commercially available dual inline package (DIP) using colloidal silver paste, with the ohmic contact face down (Figure 9). A Kulicke & Soffa wedge wire bonder was used to connect the individual, working diodes to the DIP bonding pads using 25 µm Au wire. Au wire was also connected to a DIP bonding pad and extended beneath the wafer to make a connection with the ohmic contact.

Table 2. K&S wire bonder settings

	1st	2nd
Loop	3.5	
Search	1.8	1.5
Force	4.0	4.5
Time	4.5	4.5
Power	3.3	3.3

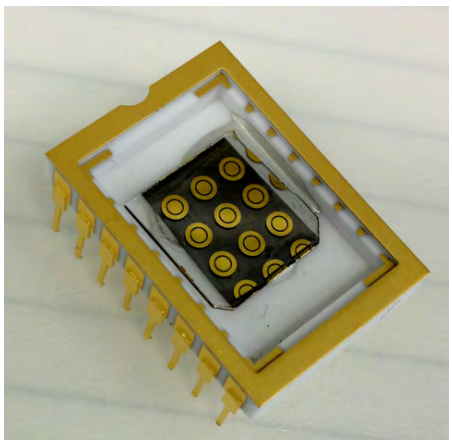

Figure 9. Final device mounted in DIP using Ag paste, ready for wire bonding.

2.3.2 Maskless Photolithography

The leakage current of Schottky barrier diodes under reverse bias is highly dependent on the surface morphology of the interface between the metal contact and semiconducting material. A smooth, defect-free surface is essential to achieving a low leakage current device. Unfortunately, the HVPE growth techniques for GaN are relatively immature, resulting in multiple "macro defects" on the wafer surface. Depositing diodes over or in close proximity to these defects typically results in non-rectifying behavior in the device, and a non-functional detector. The randomly distributed locations of these defects make photomask alignment very difficult, and often results with many diodes deposited over defects. This leads to many unusable detectors deposited using a rather expensive material (Pt or Au) on a rather expensive wafer. This issue is usually non-existent in the fabrication of detectors made from more mature semiconductors (Si, GaAs, SiC) since the epi-surface is typically defect free. A limited number of GaN wafers with exceptionally low n-type doping were procured for this project, however these wafers also exhibited an unusually high number of macro defects. Photomasks used to transfer diode and bonding pad patterns during photolithography require pre-planned designs, and are too expensive (~$500) and time intensive (2-3 week lead time) for one time use customization on these unusual wafers. An alternative cheaper and more efficient solution has been determined by utilizing a maskless aligner system for wafer patterning. The Heidelberg Instruments tabletop maskless aligner system allows for a pattern to be generated in layout software, and then transferred using a high power UV laser without the use of a photomask. Although most of the fabricated GaN devices are on the order of 0.5 mm in diameter, the system is capable of exposing features as small as 1 µm.

Since the layout pattern must be drawn before uploading to the maskless aligner, the size and position of macro defects relative to the edges of the wafer must be known in advance. A code was written using MATLAB to accomplish this objective. First, a high-resolution photograph is taken of the top surface of a GaN wafer next to a second object of known size, typically a ruler, as shown in Figure 10.

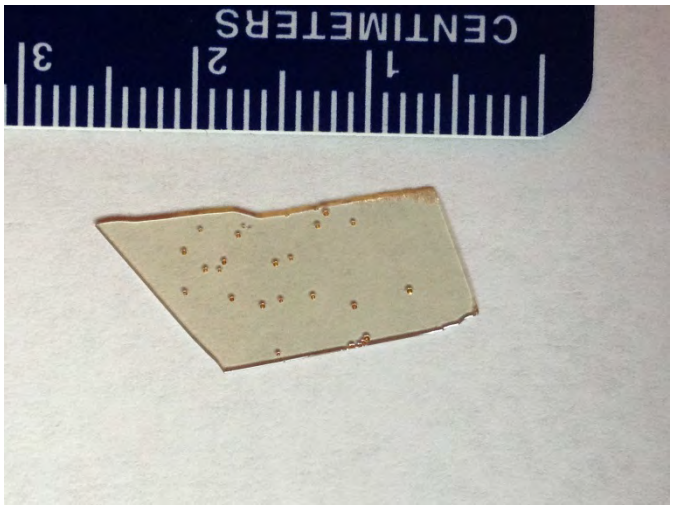

Figure 10. High resolution image of low doped GaN wafer with multiple macro defects used in maskless aligner device layout code. Ruler included for image scaling.

The MATLAB code uses the object of known size to determine a physical distance between pixels in the image. The code then utilizes several image processing functions in MATLAB to locate the boundary of the wafer as well as macro defects. The user is permitted to add or remove macro defects found by the code, to prevent shadows in the image being mistaken for actual defects. Once the necessary defects are located, they are converted from a pixel value to a physical size while maintaining their shape (Figure 11).

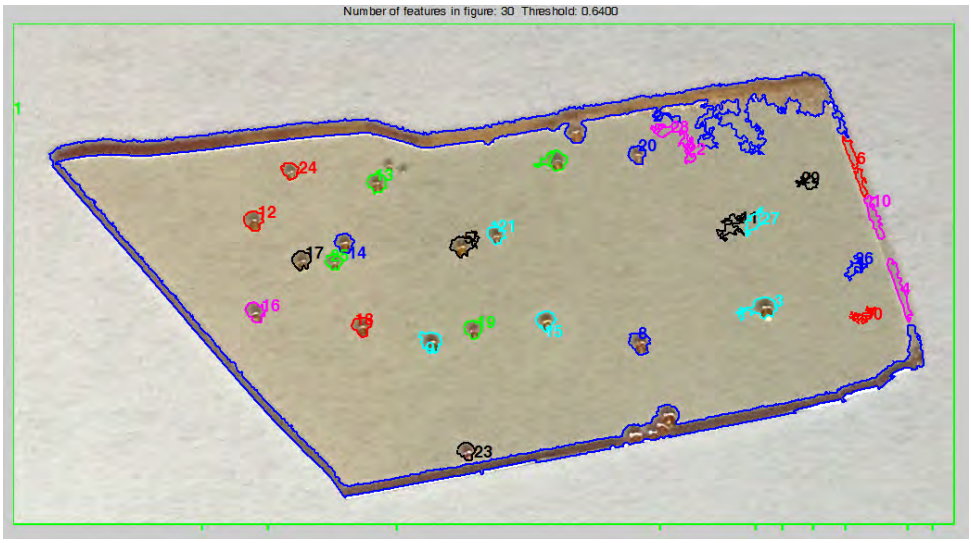

Figure 11. Code identification of wafer perimeter and defect locations. The user selects which features to include by entering the defect number, shown in the same color as the line surrounding the defect of interest.

An open source toolbox [2] is then used to convert the matrices containing the shape, size, and location of the wafer and defects into a GDS II file format, native to mask development software. This process results in a mask file containing a scaled outline of the irregularly shaped wafer and associated defects. The file can then be used by layout editing software to strategically place diodes and bonding pads which avoid macro defects, resulting in more working diodes and better utilization of the finite GaN material (Figure 12). Thin (60 µm) metal strips can also be added to the layout file as cut guides for wafer dicing, giving the operator of a dicing tool the precise locations of where to cut the wafer for device packaging.

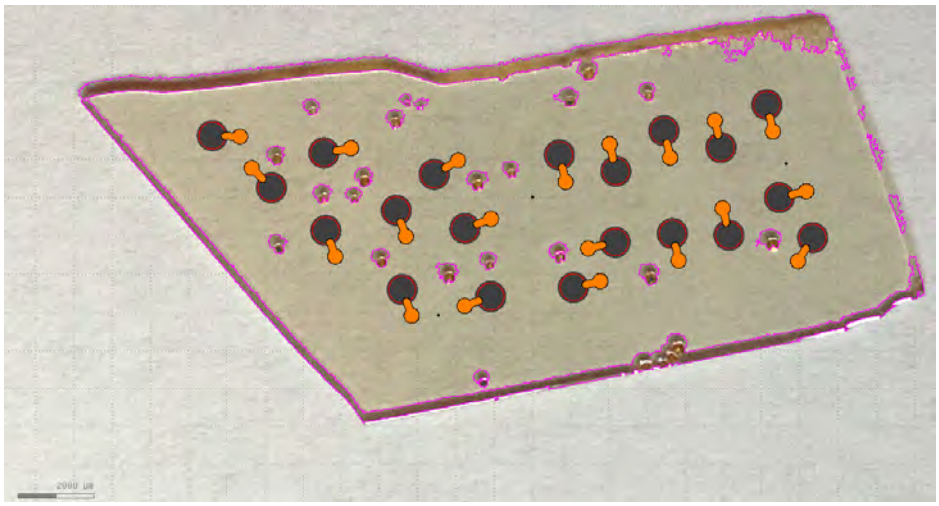

Figure 12. Placement of diodes away from macro defects on irregularly shaped wafer using maskless aligner and custom image processing scripts.

2.3.3 High Temperature Optimization

Initial high temperature tests on Ni/Au Schottky diodes showed the devices failing at temperatures over 100˚C, with leakage currents above 100 µA at 200˚C. As a result, our fabrication process was modified to reduce leakage current in the detectors. N-GaN wafers with exceptionally low doping levels were also requested from Kyma to improve detector performance.

The first modification was to use a different metal for the Schottky contacts. Other researchers [3] have found that Schottky contacts made of Ni on bulk n-GaN can diffuse into the device when exposed to high temperatures, resulting in the loss of the contact's rectifying behavior. Pt was chosen as the new contact material for several reasons. First, the higher melting point and refractory nature of Pt should theoretically reduce diffusion of the metal into the device at high temperatures. Secondly, Pt has a slightly higher work function than Ni (5.65 eV vs. 5.15 eV), leading to a higher Schottky barrier height and reduced leakage current. Finally, Pt can be present on the wafer when used in an ICP-RIE while Au cannot be exposed in the instrument.

A second modification to the detector design was a passivation layer over the exposed GaN material, intended to reduce surface leakage current in the device. SiN_x was chosen for the passivation layer, as this material has been shown to reduce leakage current and increase breakdown voltages in AlGaN\GaN High Electron Mobility Transistors (HEMT) [4]. SiN deposition was performed via Plamsa Enhanced Chemical Vapor Deposition (PECVD), with openings subsequently etched via ICP-RIE.

2.3.4 Wafer Dicing

Isolation of groups of detectors was accomplished using a K&S 7100 Precision Dicing Saw. The saw was a recent addition to the clean room user facility, and as such it had not been used for dicing GaN. Dozens of GaN samples and several months were spent to formulate a cutting recipe for the fabricated GaN detectors, at the expense of several

batches of working devices. A recipe was finally reached, using a bonded diamond grit blade (Disco: ZH05-SD2000-N1-70) with a 30,000 rpm spindle speed, and 3 mm/s feed rate, cutting 50 µm deep per pass. Typically 9 passes were required to completely traverse the wafer, with chipping occurring ≈1 mm on either side of the cut.

2.3.5 Electrical Characteristics

I-V measurements were performed using a Keithley 2400 SourceMeter to characterize the leakage current in the detectors over a range of reverse biases (Figure 13). Initial I-V measurements were extended to reverse the bias voltages high enough to cause breakdown in the device. However, many devices exhibited breakdown at voltages far below the theoretical breakdown electric field for GaN (3.3×10^6 V/cm), resulting in the permanent destruction of diodes. This damage was likely due to activation of leakage paths along dislocations or micropipes in the material. Thus, in an effort to minimize destruction of the detectors before radiation characterization could occur, biasing of these devices was limited to below 20 V.

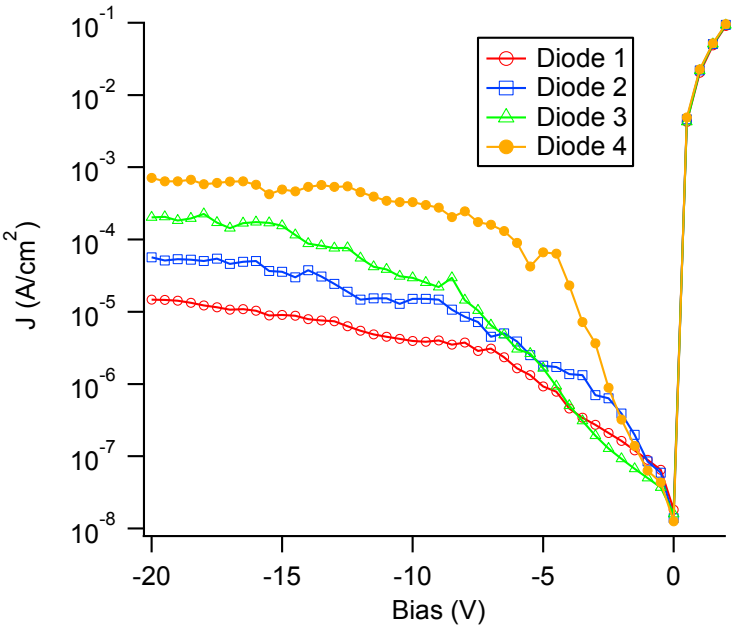

Figure 13. I-V measurements from unintentionally doped GaN detectors.

As Figure 13 shows, the current density in these detectors was rather high. However, due to the small area of the detectors (0.0079 cm^2), the actual leakage current was sufficiently low to be used in radiation detection. Capacitance-Voltage (C-V) measurements were also performed on the devices using a 1 MHz Boonton 7200 capacitance meter. Results of the C-V measurements were used to determine the depletion depth of the detectors while under reverse bias (Figure 14). Measurements indicated that the detectors did not deplete much beyond 1 µm when fully reverse biased, due to the high doping of the material (Figure 15).

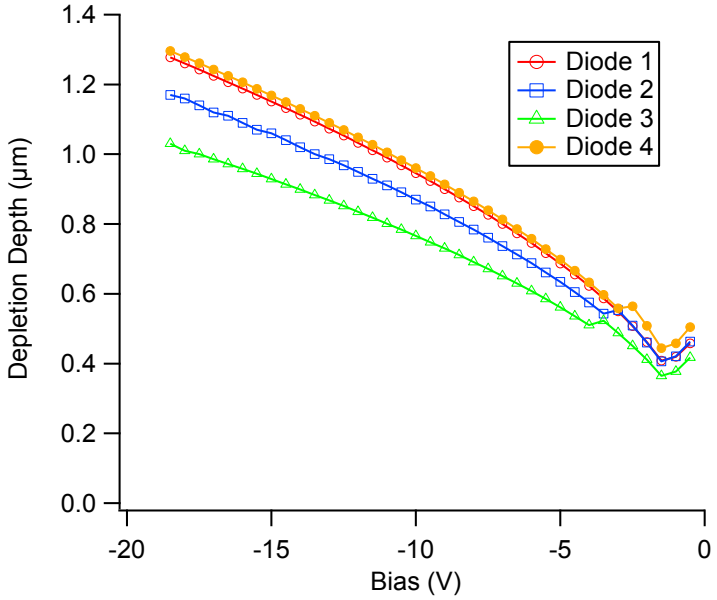

Figure 14. Depletion depth of unintentionally doped GaN detectors calculated using C-V measurements.

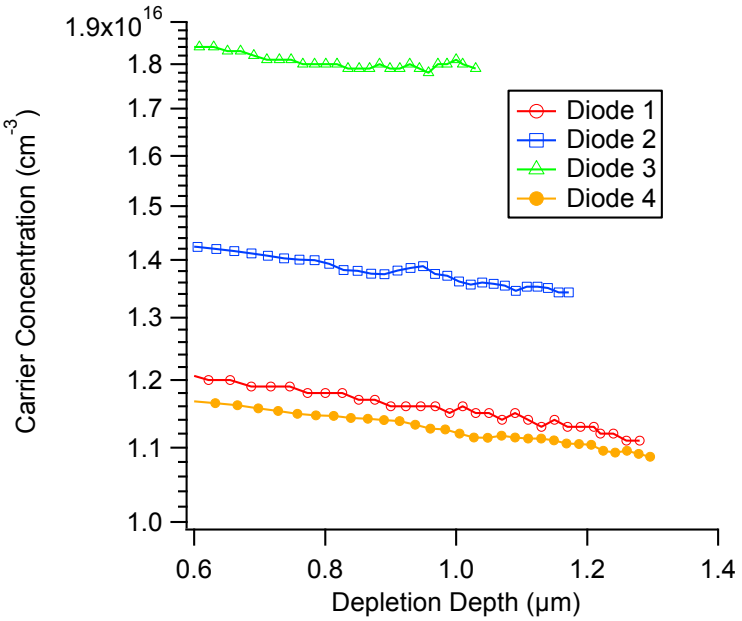

Figure 15. Carrier concentration in unintentionally doped GaN as a function of depletion depth.

GaN wafers with nominally lower doping levels were obtained later in the project, and were used to fabricate Schottky diode detectors. C-V measurements in these devices showed the carrier concentration to be ≈9 × 10^{15} cm^{-3}, and were therefore capable of wider depletion regions, up to 2 µm. Leakage current in these devices were also considerably lower, as Figure 16 depicts. Devices from the 1st generation of GaN material were used in α-particle characterization, while devices from the 2nd generation of material were used for neutron detection.

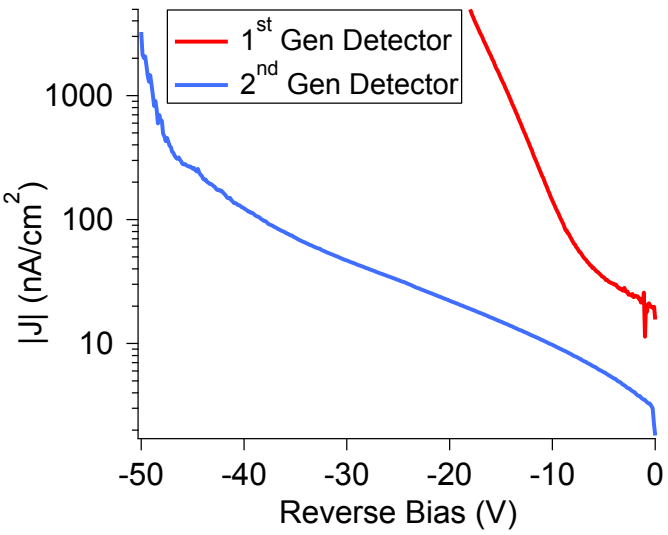

Figure 16. I-V curve for a detector fabricated from 1st generation GaN material, and 2nd generation (low doping) GaN material.

Unfortunately, passivation of the GaN surface using PECVD SiN lead to unexpected device failures. I-V measurements on the diodes before and after SiN deposition showed the formation of a heterojunction between the GaN and SiN (Figure 17). This resulted in the detectors permitting a high flow of current when the applied voltage reached the bandgap of SiN (5 eV). As a result, detectors which received a SiN passivation layer were no longer functional.

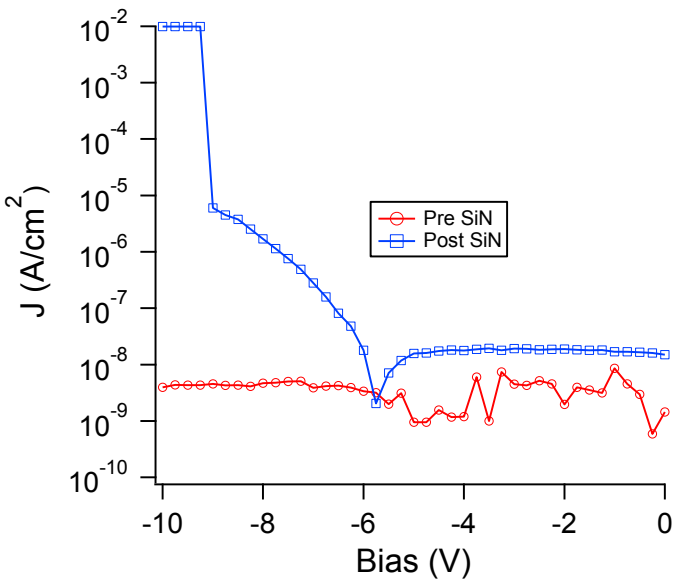

Figure 17. I-V characteristics of GaN detector before and after SiN deposition.

2.3.5.1 Expected High Temperature Performance

I-V measurements were also performed on the detectors over a range of elevated temperatures to extract several important parameters. The primary mechanism of leakage

current in a reverse biased Schottky diode is thermionic emission which can be characterized using:

$$I = I_s\left(e^{\frac{q(V-IR_s)}{nkT}} - 1\right)$$

where V is the applied bias, R_s is the series resistance of the detector, n is the ideality factor, q is the elementary charge, k is the Boltzmann constant, and T is the temperature in kelvin. I_s is the reverse saturation current in the detector and is given by:

$$I_s = AA^{**}T^2 e^{-\frac{q\Phi_B}{kT}}$$

where A is the diode area, A^{**} is the effective Richardson constant (A/cm^2T^2), and Φ_B is the barrier height. For reverse biases where $V \gg kT$, $I = -I_S$ and the leakage current becomes highly dependent on the barrier height, as this term is in the exponent. To determine the value of these parameters, forward and reverse bias I-V measurements were performed over several temperatures, ranging from 22 °C to 200 °C, as shown in Figure 18 and Figure 19.

There are many different methods to determine the saturation current (I_S), series resistance (R_S) and ideality factor (n) of a diode. The barrier height is then calculated using these determined values and an assumed effective Richardson constant. Since the effective Richardson constant can vary depending on diode fabrication techniques, using an assumed effective Richardson constant introduces error into the barrier height calculation. If forward I-V measurements are available at several different temperatures, the effective Richardson constant (A^{**}) and barrier height (Φ_B) can be determined using a modified Norde plot. The modified Norde plot requires only the ideality factor for the barrier height determination.

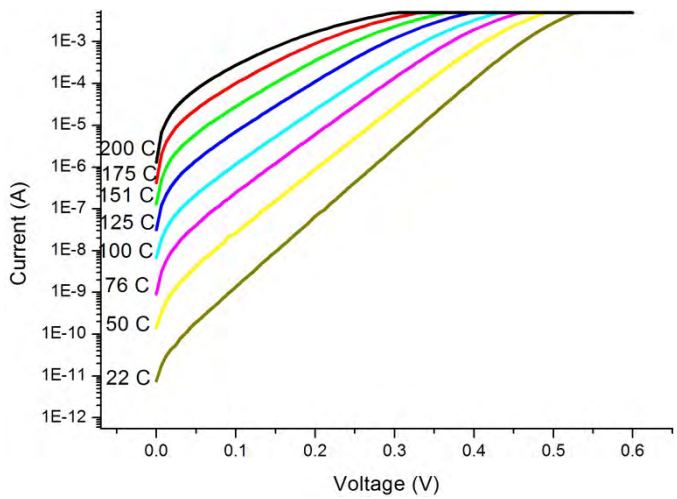

Figure 18. Forward biased I-V measurements obtained from detectors at several temperatures.

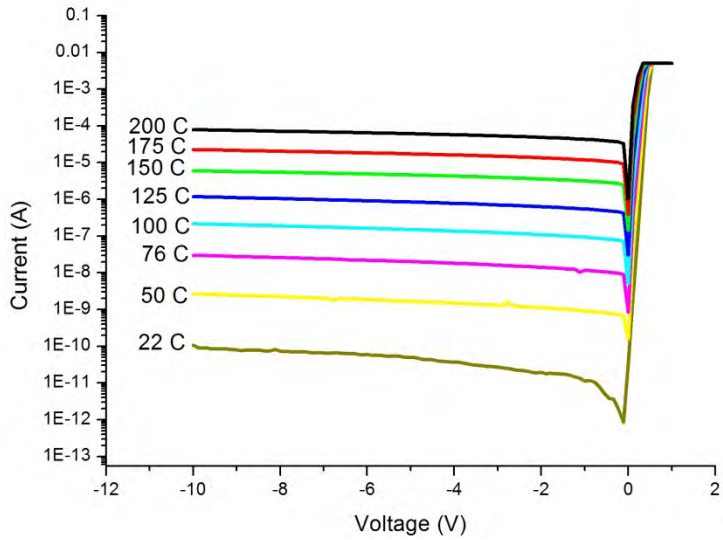

Figure 19. Reverse biased I-V measurements obtained from detectors at several temperatures.

The ideality factor and series resistance were determined using several different methods, summarized below in Table 3. The extracted parameters for forward bias measurements performed at 22 °C are summarized in Table 4.

Using the previously calculated ideality factor and forward bias measurements at several temperatures, a modified Norde plot was constructed to give $A^{**} = 20.5\, A/cm^2K^2$, and $\Phi_B = 0.85\, V$. The modified Norde plot of forward bias I-V measurement is shown in Figure 20. Using these values, the theoretical reverse saturation current was plotted against the measured leakage current for several temperatures (Figure 21). The close correlation between the theoretical and experimental values indicates that thermionic emission is the primary mechanism for leakage current in the detectors. The theoretical reverse saturation current was then extended to temperatures of 800 °C, to give an estimate of how much current can be expected at high temperatures. Several additional plots were added to Figure 21 to show how the leakage current could be reduced with a larger barrier height. The barrier height could be increased in the detectors through improved surface preparation or use of a metal with a higher work function, such as platinum.

Table 3. Methods to determine S_R and n in detectors.

Method	Graphical Approach
1	$I\frac{dV}{dI}$ vs. I
2	$\log(I)$ vs. V
3	$\frac{dV}{dI}$ vs. $\frac{1}{I}$
4 (Cheung's Method [5])	$\frac{dV}{d(logI)}$ vs. $IR_S + n\frac{kT}{q}$

Table 4. S_R and n parameters extracted using various methods.

Method	R (Ω)	n
1	5.94	1.16
2	N/A	1.05
3	5.88	1.16
4	5.95	1.03

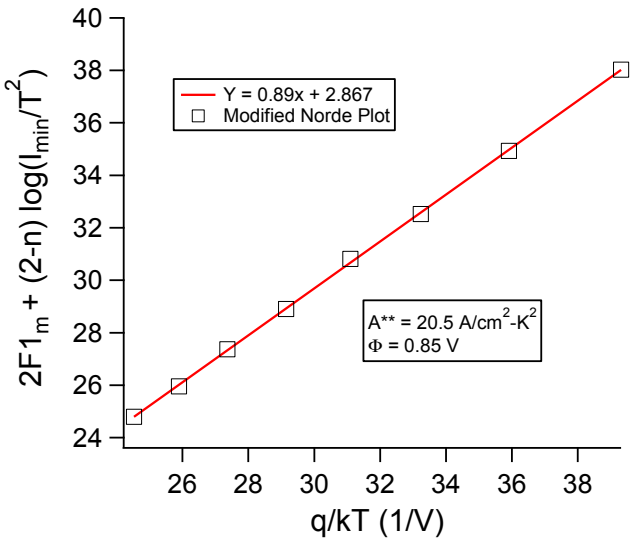

Figure 20. Modified Norde plot of forward bias I-V measurements.

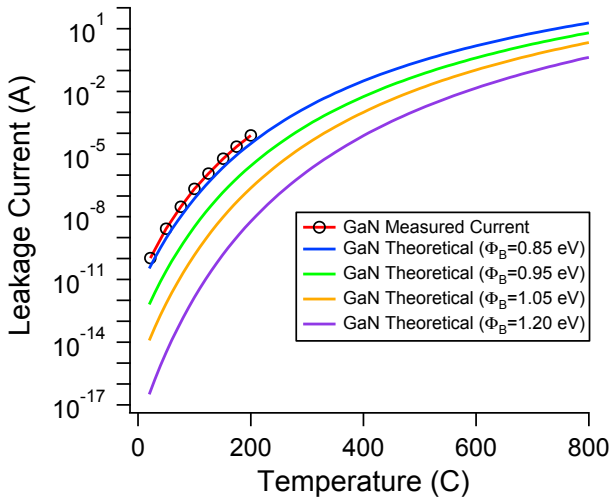

Figure 21. Theoretical vs. experimental leakage current in GaN detectors for high temperature operation.

2.3.6 Radiation Response

The working detectors were then evaluated for their response to radiation. Alpha particles from an 0.8 μCi ^{241}Am source were first used to elicit a response from the detectors. Later, γ and β-particles were used to characterize the detectors.

2.3.6.1 Alpha Particle Detection

Pulses due to alpha particles were observed in several detectors immediately following commencement of data acquisition. Devices were biased to -20 V for the majority of testing, to maximize the detector's depletion depth without damaging the device or producing unacceptably high leakage current in the device. Although pulses were easily observed, when the digitizer was placed in histogram mode severe ringing was observed in the spectra, with multiple peaks appearing at evenly spaced intervals. Several modifications to the signal path to reduce this ringing, and an experiment was performed to verify that peaks observed in the histogram were in fact due to alpha particles.

First, the source and detector were aligned such that the surface of the disk source and surface of the detector were parallel and centered over one another. The distance between detector and source was precisely measured, along with the diameter of the disk source and detector to allow for a calculation of the theoretical count rate in the detector. Using the known activity (A=34.31 kBq), radius of the source (s=4 mm), and radius of the detector (a=0.5 mm), the solid angle (Ω) and count rate (N) were calculated using:

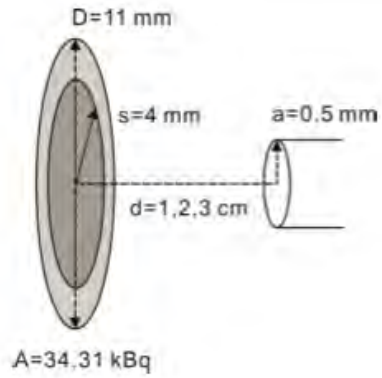

$$\Omega = \frac{4\pi a}{s}\int_0^\infty \frac{e^{(-d\cdot k)} J_1(s\cdot k) J_1(a\cdot k)}{k} dk$$

$$N = S * A \frac{\Omega}{4\pi} \varepsilon_{in}$$

where S is the branch ratio of alpha emission in ^{241}Am (100%), and ε_{in} is the intrinsic detection efficiency for alpha particles in GaN (assumed to be 100%). Multiple spectra with the source placed 1.5 cm, 2.5 cm, and 3.5 cm from the detector were acquired to generate Figure 22.

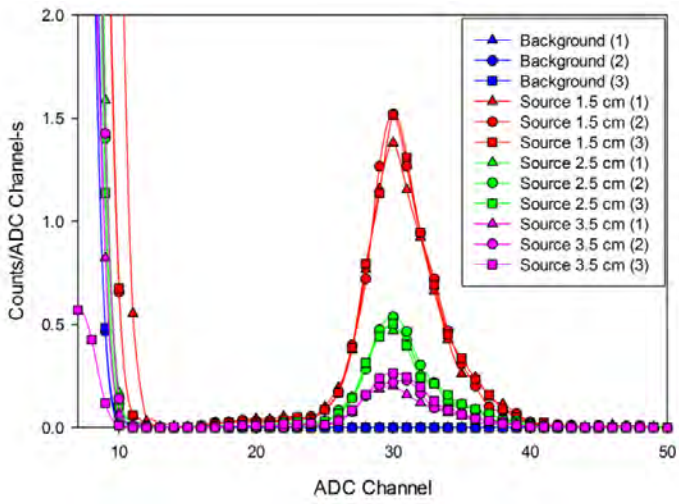

Figure 22. Alpha particle spectra acquired in GaN detector with various source-detector spacing.

Counts for each acquisition were normalized to their respective count times, and counts in the peak for each source/detector distance were integrated to give a total count rate in the detector. Using the previously stated methods for determining the theoretical count rate, the experimental and theoretical rates were compared, as shown in Figure 23.

The results indicated a strong correlation between the theoretical count rate in our detector and the experimental count rate, with the theoretical count rate falling within the error bars of the experimental count rate. This indicates that the source of the pulses in the detectors followed a $\approx r^{-2}$ relationship, leading us to conclude that the pulses were due to a radiation source. However, since ^{241}Am also emits a 59 keV γ-ray, further testing was required to prove that the pulses in the detectors were due to alpha particles, not γ-rays. This was accomplished by placing a 30 µm thick sheet of Al between the source and detector. SRIM [6] calculations predict the range of 5.48 MeV α-particles in Al to be approximately 24 µm, making the thin foil sufficiently thick for stopping incident alpha particles. However, such a thin foil attenuates less than 1% of the 59 keV γ-rays from the ^{241}Am source. When the foil was placed between the source and detector, the spectra was completely eliminated, indicating that the GaN detector is sensitive to alpha particles, but not γ-rays.

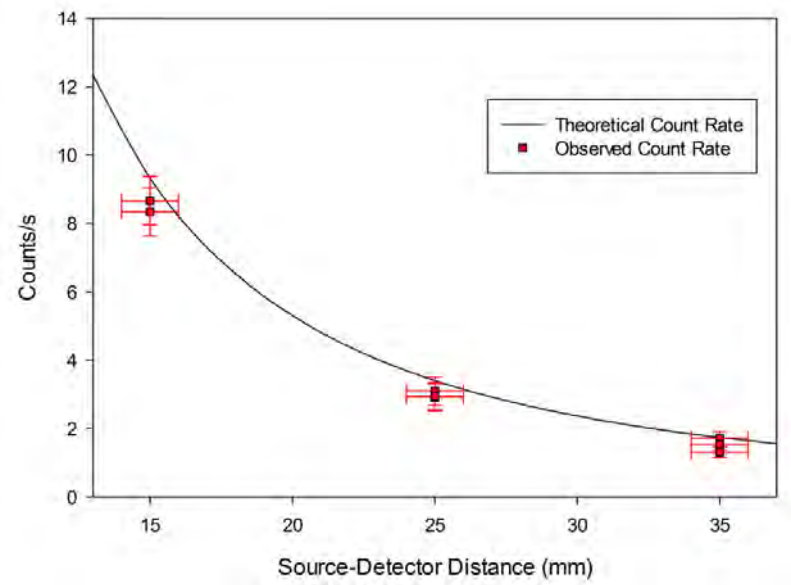

Figure 23. Theoretical count rate vs experimental count rate in GaN detectors for 3 source-detector distances.

2.3.6.2 Gamma and Beta Detection

Experiments were conducted with the GaN detectors to characterize the γ and β response using several sources. γ-rays from a ^{57}Co, Co^{60}, and the previously mentioned 59 keV ^{241}Am source, however there were no pulses detected in the device. A ^{14}C β-source was also used in vacuum for spectrum acquisition, as expected, the pulses were not detected. It was therefore confirmed, that due to the low Z numbers for GaN (31 and 7), and the shallow depletion depth in the device, the detectors are only responsive to high Linear Energy Transfer (LET) radiation, such as α-particles, tritons, and protons.

2.3.6.3 Charge Collection Efficiency

The charge collection efficiency (CCE) of the detector was analyzed using α-particle spectra collected over several reverse bias voltages, ranging from 4 to 18 V (Figure 24). Low energy noise in the detector prevented the acquisition of spectra for biases below 4 V. As anticipated, increasing the bias voltage resulted in the centroid of the spectra shifting to higher energies. This is due to the depletion region expanding at higher voltages, resulting in the collection of more e-h pairs generated by the incident α-particles.

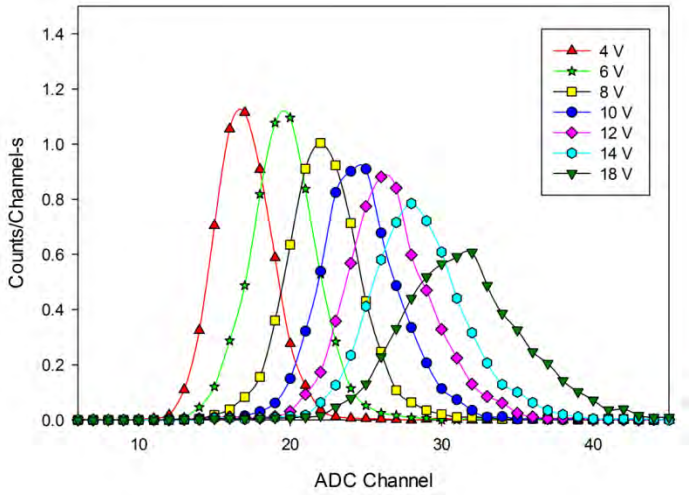

Figure 24. ^{241}Am alpha spectra acquired in GaN detector over several reverse bias voltages.

However, the spectra also tended to broaden as the reverse bias increased. This phenomena could be attributed to several different mechanisms. One reason for the spectral broadening could be due to the inclusion of more trapping sites as more of the detector is depleted, resulting in incomplete charge collection and varying pulse heights. The broadening could also be attributed to a wider range of α-particle path lengths as the geometry of the depletion region changes, allowing some particles to traverse the depletion region at an angle, while other particles take route perpendicular to the detector surface. Finally, the broadening could be due to charge accumulation in the device. Electron-hole pairs generated could become trapped in the GaN material after extended periods of exposure, distorting the electric field locally. Since the spectra was acquired sequentially and in order of increasing reverse bias, more alpha exposure occurred for higher reverse bias than lower reverse bias. Thus, the 18 V experiment occurred last, after the detector was exposed to α-particles for several hours, and could account for the peak broadening. However, the first two explanations are the most probable, as the activity of the α-source was quite low (0.8 μCi).

To perform an energy calibration of the acquired spectra, a reference Si detector was used. The Ortec ULTRA Ion-Implanted Silicon charged particle detectors have a 100 μm depletion depth, beyond the range of 5.48 MeV α-particles in Si, allowing for absorption of the entire particle energy. Spectra was acquired in the Si detector using the 5.48 MeV α-particles from ^{241}Am, along with the 59 keV γ from ^{241}Am, the 122 keV γ from ^{57}Co, and the 157 keV β from ^{14}C. 10 μm and 20 μm Al foils were also used to reduce the energy of the 5.48 MeV α-particles from ^{241}Am down to 3.76 MeV and 1.42 MeV respectively, seen in Figure 25. The energies of these two α-particles were determined using a TRIM simulation, and finding the centroid of the simulated spectra.

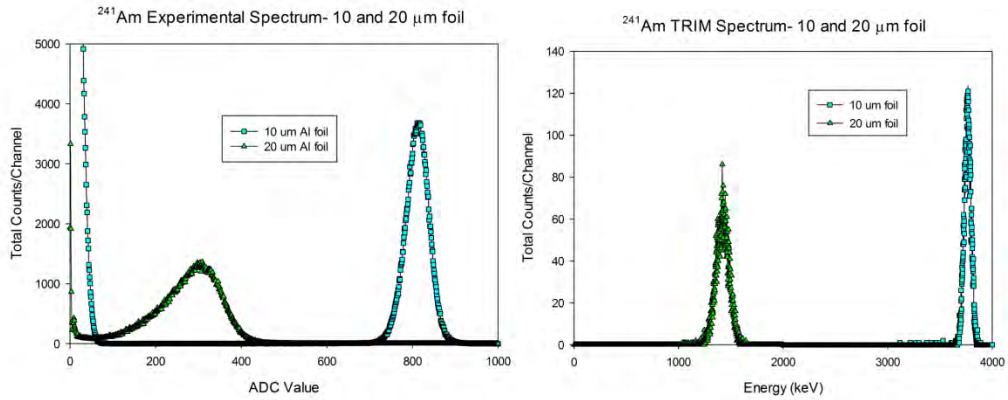

Figure 25. Experimental (left) and TRIM simulation (right) of 5.48 MeV α-particles after traversing a 10 µm and 20 µm Al foil, creating 3.76 MeV and 1.42 MeV particles.

Spectra from the previously mentioned sources were then used to perform an energy calibration in the Si detector, assuming a linear relationship between energy and ADC channel (Figure 26). The energy calibration for the GaN detector was then calculated by multiplying the Si calibration curve by the ratio of e-h pair creation energy in GaN to that in Si (8.9/3.6 eV).

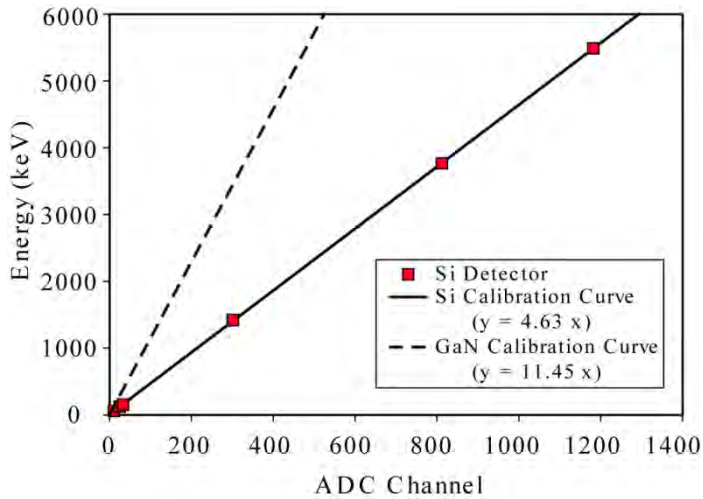

Figure 26. Calibration in reference Si detector and corresponding GaN calibration curve.

Using a derived energy to channel factor of 11.45 eV/Chnl, the spectra of Figure 24 were calibrated to energy, generating Figure 27. The CCE of the detector was then analyzed, by dividing the charged measured by the charge generated in the detector.

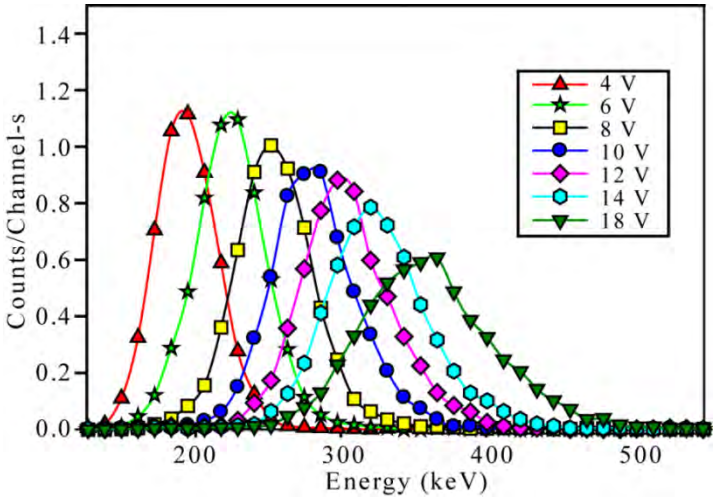

Figure 27. Energy calibrated alpha spectra over a range of reverse bias voltages.

Two methods were considered to calculate the CCE of the device. In a previous study on CdZnTe [7], the device CCE for a partially depleted detector was assessed by considering the energy deposited solely in the depletion region. Because the thin depletion region formed in bulk GaN is similar to that of the CdZnTe Schottky device structure, the CCE of our device was evaluated in the same manner. The peak energy of the alpha particle spectrum at a given reverse bias voltage was divided by the theoretical energy deposited in the depletion region formed under the same voltage. The theoretical energy deposited was calculated by assuming a full depletion approximation between the depletion region and bulk GaN material. Using the doping level N_d and built-in potential V_{bi}, calculated from C-V measurements, the depletion depth for a given reverse bias voltage was determined using:

$$X_d = \left[\frac{2\epsilon_{GaN}(V_{bi} + V_R)}{qN_d}\right]^{\frac{1}{2}}$$

where X_d is the depletion depth, ϵ_{GaN} is the relative permittivity of GaN, V_R is the applied bias, and q is the elementary charge. The stopping power for α-particles in GaN was then determined using SRIM, allowing for the calculation of energy lost in the depletion region of known thickness.

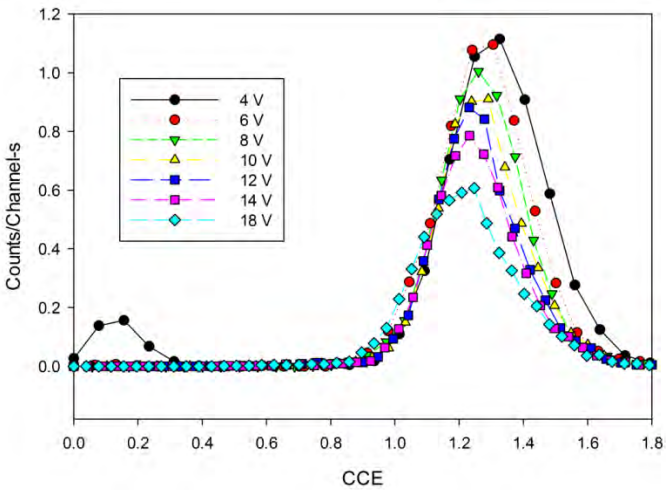

Figure 28. CCE for several reverse biases, calculated using charge generated in the depletion region only.

This analysis gave a CCE of over 100% for all reverse biases (Figure 28). While this may appear as an anomaly, the additional charge collected was later analyzed using Synopsis TCAD and attributed to hole impact ionizations in the depletion region, which generate additional e-h pairs, and electron diffusion from the undepleted region.

It is noteworthy that other researchers [8] who have developed thin-film GaN (up to 12 µm) on a foreign substrate have chosen to determine the CCE by using the energy deposited in the detector as a whole. With this definition, our device's CCE was only 3–6% (Figure 29), depending on the applied reverse bias, due to the fact that only a fraction of the particle's energy is deposited in the SCR before being fully stopped in the bulk GaN.

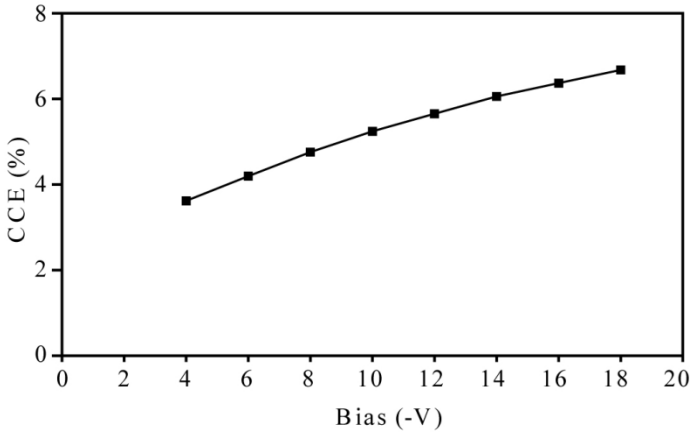

Figure 29. CCE using charge generated in bulk detector for ^{241}Am α-particles.

3. TCAD Simulation

Several simulations were performed using the Synopsys Sentaurus device simulation software. An investigation into the electric field, charge recombination, and the deconvolution of charge collection in the device was completed.

3.1.1 Built-in Electric Field

The simulated built-in electric field within the depletion region is shown in Figure 30. The intercept of the curves with the x-axis indicates the depletion depth. Under these bias conditions, the field in the depletion region is significantly larger than the undepleted region. The magnitude of the depletion region field is proportional to the applied voltage and decreases linearly from the Schottky side to the edge of the depletion region. Further simulations indicate that for bias voltages up to 160 V, both the electrons and holes have not yet reached their saturation velocities. However, at a certain bias voltage, the electron velocity is almost constant within the depletion region, and hole velocity is linearly decreasing from the Schottky contact to the depletion edge.

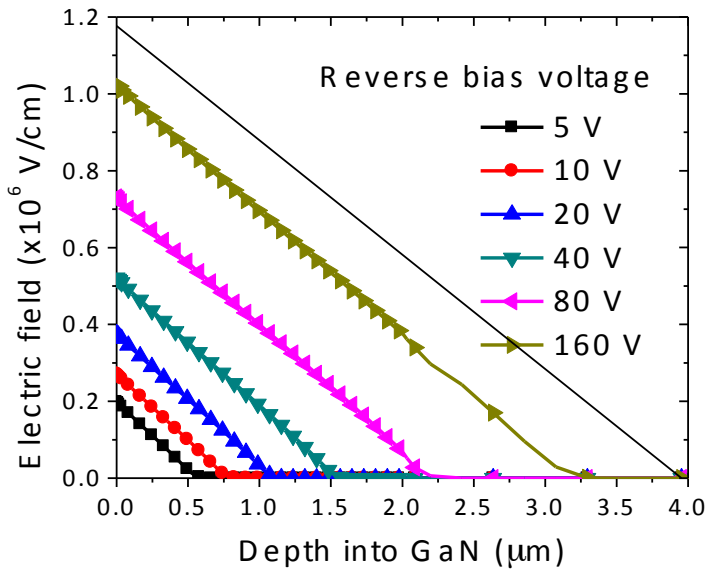

Figure 30. Simulated built-in electric field in the depletion region.

3.1.2 Impact Ionization, Recombination and Trapping

At a reverse bias of 18 V, when the hole current density reaches its maximum (~5.2 ns), Figure 31 (a), (b), and (c) show the impact ionization caused by electrons, holes and their sum, respectively. The impact ionization is only present in the depletion region below the Schottky contact, in close proximity to the incident alpha particle, where a large number of primary carriers are created and a large electric field is present. Surprisingly, the majority of secondary e-h pairs generated is due to hole impact ionization. This is a result of the relatively small drift length of holes compared with electrons.

Figure 32 (a), (b), and (c) simulate the results of band-to-band radiative recombination, Shockley-Read-Hall (SRH) trap-assisted recombination, and band-to-band Auger recombination. Recombination occurs along the entire particle trajectory. Radiative recombination is the dominate carrier loss process, which is several orders of magnitude higher than the other two processes. This is expected in a high purity, direct band semiconductor.

Figure 33 and 34 show the occupancy dynamics for hole trap H2 and electron trap L1, respectively. Generally, the trapping dynamics are much faster for holes than electrons, and the dynamics in the depletion region are different from the undepleted region. In the undepleted region, after the alpha particle impact, the hole traps go through a fast-trapping, slow-detrapping process, which takes about 4 ps and 20 ns, respectively. The electrons go through a fast-detrapping, slow-retrapping process, which takes about 6 ns and 1 μs respectively. In addition, only 80% of the electron traps can be occupied. In the depletion region, the trapping-detraping process occurs much slower.

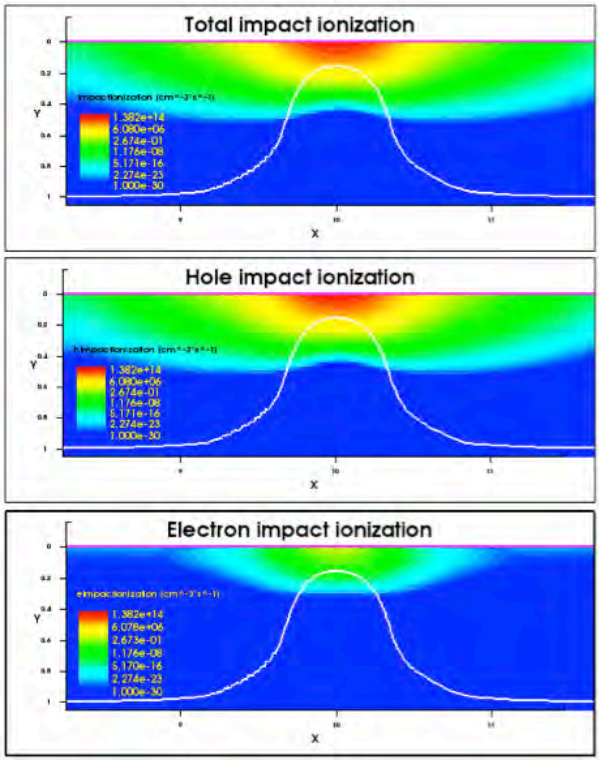

Figure 31. Impact ionization caused by (a) holes, (b) electrons, and (c) sum of holes and electrons, plots are generated when the diode is reverse bias at 18V, at transient time of 5.2 ns.

Initially in the undepleted region, a large electron background is present with significantly fewer holes. Thus a large amount of electron traps are occupied (80% according to the simulation), and the hole traps are not occupied. Subsequently, the incident charged particle generates many electrons and holes in the depletion region. Holes are trapped by the hole traps, and then detraped by recombination with the electron background. However, the trapped electrons are liberated using the deposited energy from the alpha particle, since less energy is required to liberate the trapped electrons within

the band gap than the electrons in the GaN valence band. Thus, electron traps first undergo a detrapping proces. In the depletion region, the detrapping process for both holes and electrons is characterized by a detraping constant, which is slower than in the undepleted region due to the lack of excess carriers present (since they are quickly swept away by the high built-in electric field).

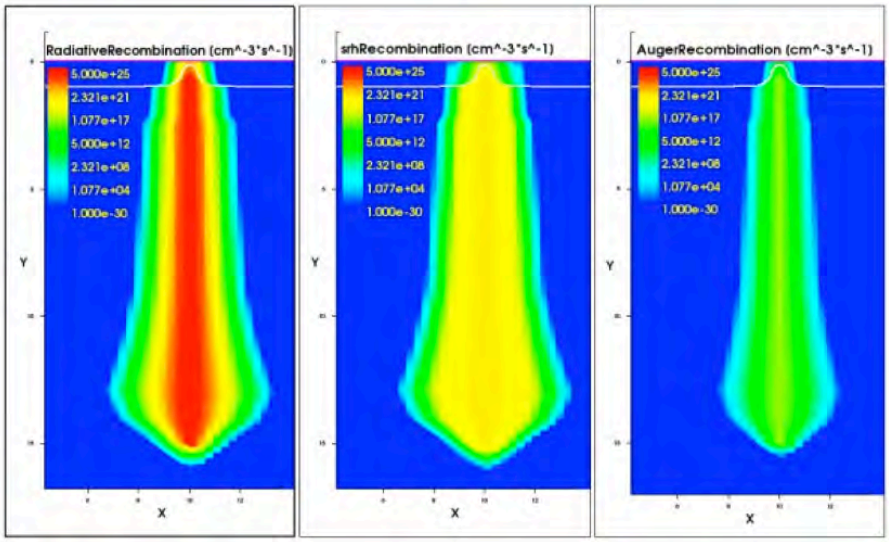

Figure 32. Carrier recombination due to and (a) Radiative, (b) SRH, and (c) Auger, plots are generated when the diode is reverse bias at 18V, at transient time of 5.2 ns.

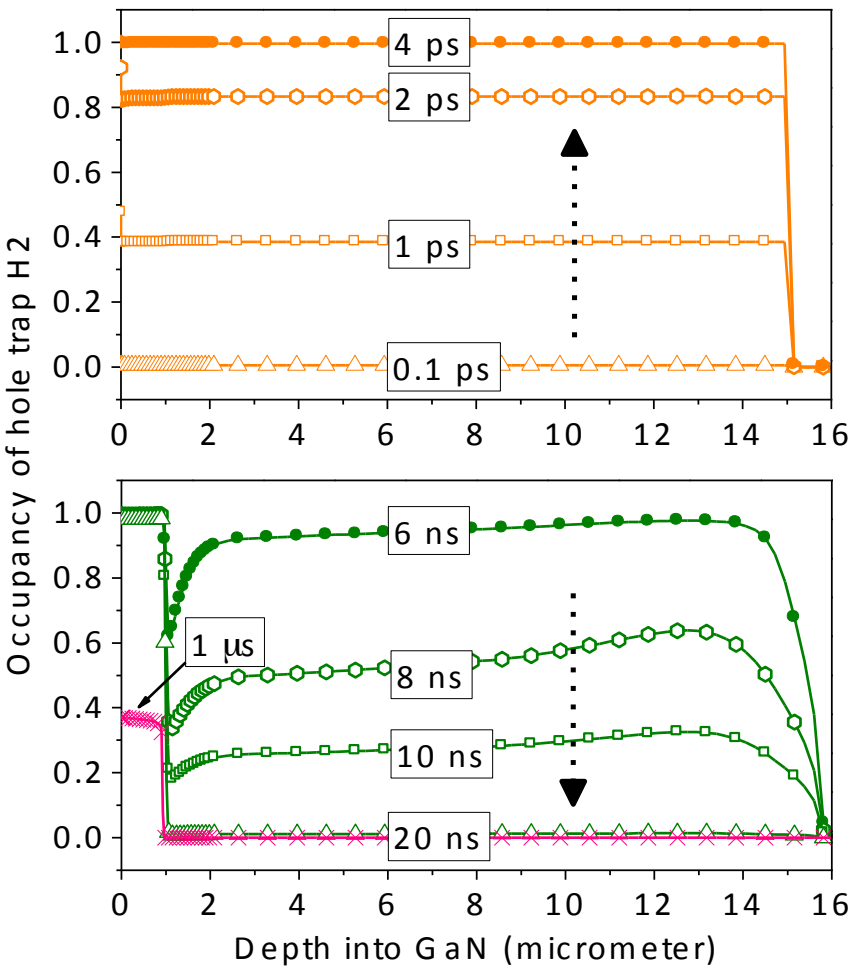

Figure 33. Hole trap H2 occupancy at different transient times.

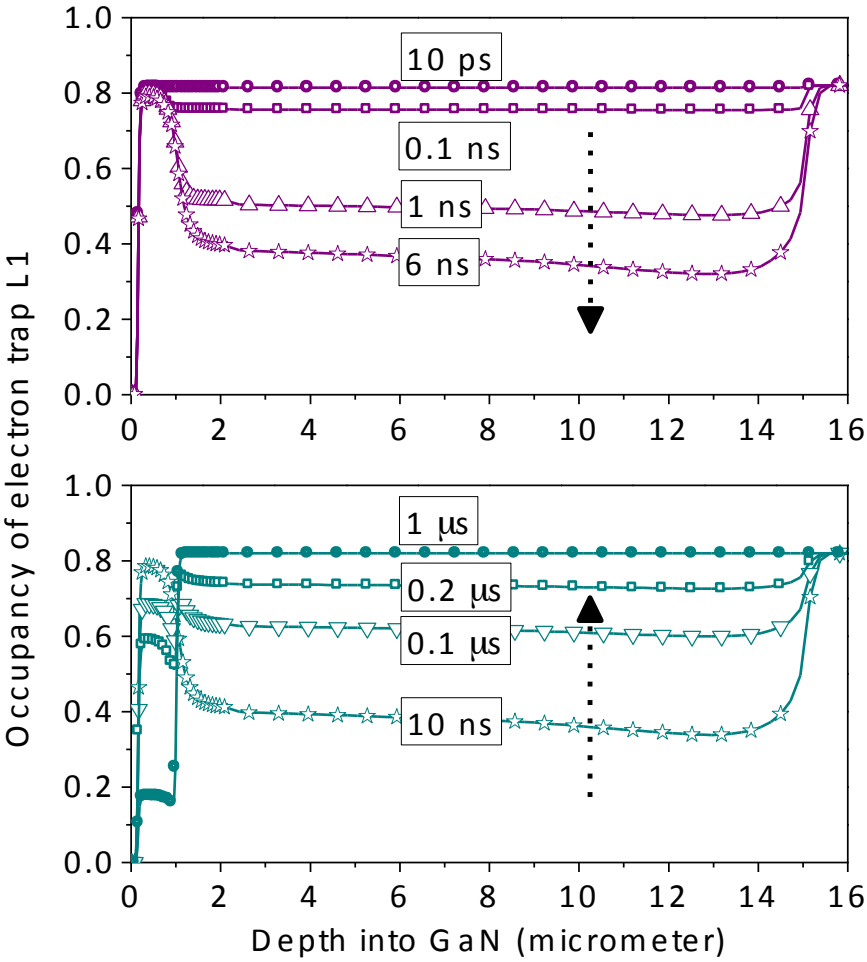

Figure 34. Electron trap L1 occupancy at different transient times.

3.1.3 Collected Charge Deconvolution

Figure 35 summarizes the contribution of different carrier components to the collected charge. The blue line shows the deposited charge in the depletion region from the 5.4 MeV alpha particle, which is obtained by SRIM simulations and incorporated into the TCAD code. By calculating the deposited charge and injecting this into the depletion region, the collected charge can be obtained (red curve). The collected charge is higher than the deposited charge due to the contributions of impact ionization in the depletion region (magenta curve). The total collected charge (black curve) is composed of the charge collected in the depletion region (red curve) and the undepleted region (green curve). Without the presence of hole traps, the collected charge in the simulation could be further increased (orange curve), due to the fact that the total collection time in the simulation is 5 ns and the trapped holes have not been released before the end of the collection process. The extra carriers generated from impact ionization in the depletion region and diffusion from the undepleted region is higher than the loss due to hole traps. Thus, if only the depletion region is used as the detector region, then the CCE is over 100%, which is consistent with previous experimental measurements. In addition, when the voltage is increased, more carriers from the undepleted region are collected, which generates a high energy tail on the peak of alpha

spectra (a phenomenon which has been observed in our detectors). The results indicate that for Schottky diode detectors fabricated on moderately doped semiconductors (~10^{16} cm^{-3} in our case), the carrier generation due to impact ionization and carrier loss due to hole traps are negligible, and the drift carriers in the depletion region is the major component of the collected charges. Thus in order to increase the charge collection efficiency, a low doping material must be used to maximize the thickness of the depletion region.

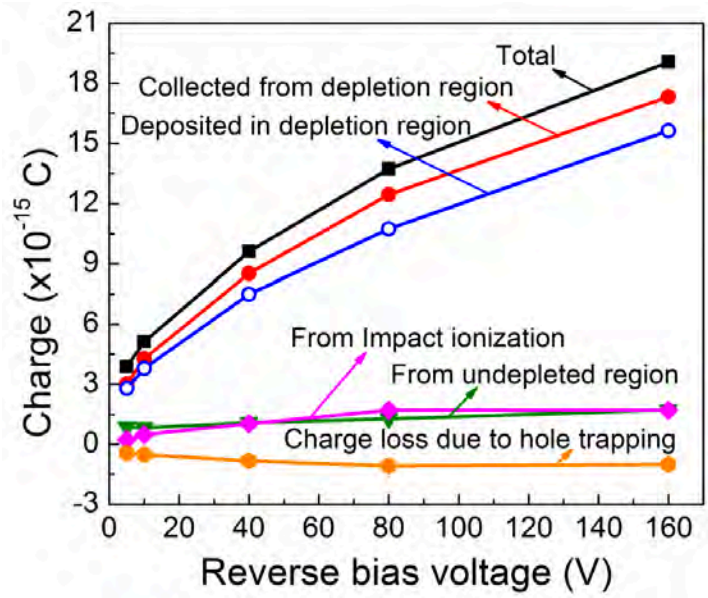

Figure 35. Contributions of different carrier components to the total collected charge, total means the total charge (holes) collected on the Schottky contact, and these charges come from the sum of both the depletion region and the undepleted region.

4. Neutron Detection

4.1 Neutron Detection in High Flux

The detectors responsive to alpha particles were used to detect thermal neutrons at The Ohio State University Research Reactor (OSURR). The OSURR is a 500 kW thermal, light water reactor with two radial beam ports. A neutron collimator composed of polycrystalline bismuth, single crystal sapphire, and apertures of lead, borated polyethylene, and borated aluminum directs and shapes a beam of thermal neutrons through one of the reactor beam ports into the beam experimentation facility (Figure 36). A large (61 cm x 61 cm right circular cylinder) vacuum chamber with 2 thin aluminum (~60 µm) entrance and exit windows is centered in the beam line for neutron experiments.

A GaN wafer with multiple detectors was wire bonded in a DIP and placed in the neutron beam facility vacuum chamber. Two of the detectors on the wafer were connected to separate preamplifiers and data acquisition channels in the digitizer. A 1 mm thick Teflon film with a ~4 mm aperture was placed 5 mm over the wafer, leaving one detector uncovered while a second detector was completely shielded by the Teflon film (Figure 37). Approximately 1 cm above the Teflon aperture, a 0.3 mm thick LiF neutron conversion film enriched to 96% ^{6}Li was mounted directly above the uncovered detector. This assembly was then centered in the neutron beam for neutron detection experiments. Following neutron capture in ^{6}Li (σ_a = 940 b), triton and alpha particles are emitted with discreet energies:

$$^{6}Li + n \rightarrow \ ^{4}He(2055\ keV) + \ ^{3}H(2727\ keV)$$

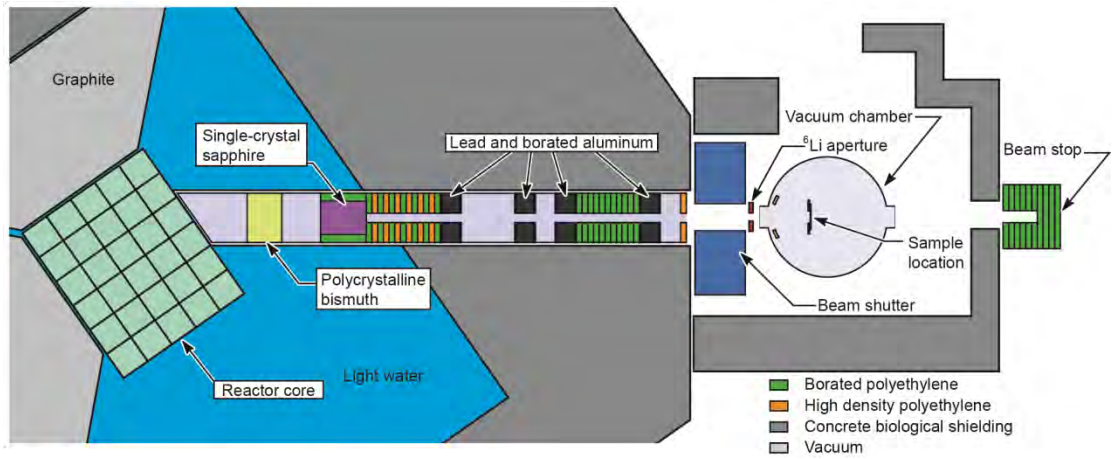

Figure 36. Schematic of neutron beam facility and sample location.

These particles travel freely to the uncovered detector, but are stopped by the Teflon film over the covered detector. Thus, only one detector (uncovered) operates via indirect-conversion by responding to charged particles emitted from neutron capture in ^{6}Li. Both detectors also exhibit a direct-conversion response to neutron capture in ^{14}N:

$$^{14}N + n \rightarrow \ ^{14}C(42\ keV) + \ ^{1}H(584\ keV)$$

However, due to the small cross section of ^{14}N (σ_a = 1.8 b), pulses from this reaction in

the uncovered detector were negligible compared to the ^{6}Li generated pulses. With the reactor operating at 50% power, both detectors were subjected to the same neutron flux (4.3×10^{6} n/cm^{2}-s) and gamma exposure (1.2 R/hr) for 51 minutes in the beam.

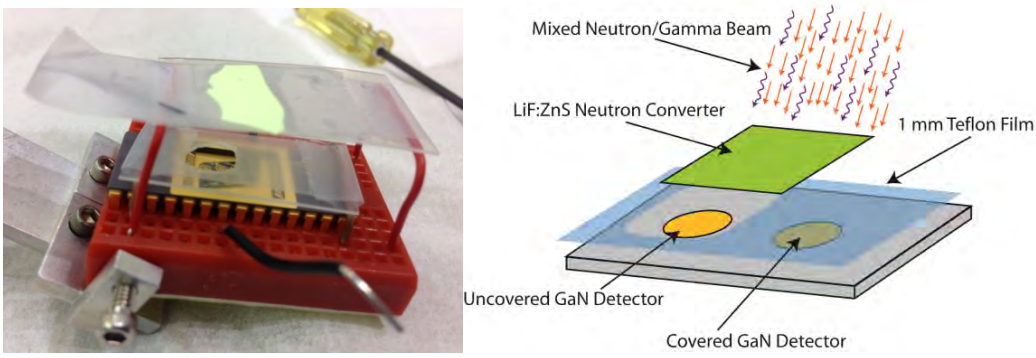

Figure 37. Picture of experimental setup (left) and device schematic (right) for GaN neutron detection experiment.

Results of the experiment showed a clear neutron response in the uncovered detector, with the peaks of the triton and alpha particle appearing distinct from one another, as shown in Figure 38. The covered detector exhibited a much more attenuated response, as expected. This detector showed a low count rate over a range of energies, stretching from 0 to ≈ 630 keV, indicative of a ^{14}N neutron capture reaction.

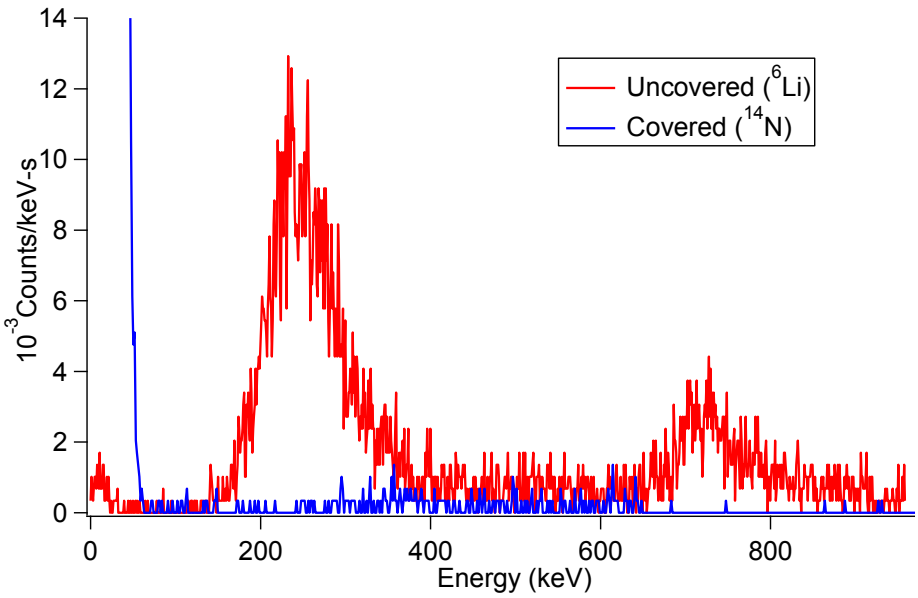

Figure 38. Spectra generated from neutron interactions in uncovered (^{6}Li) and covered (^{14}N) detectors.

An energy calibration was performed on the acquired spectra by determining the stopping power of the triton and α-particles in the GaN detector, and converting these values to residual energy as a function of depth in GaN. By knowing the depletion depth of the uncovered detector, the energy deposited by each particle can be determined and used

to calibrate the spectra. Although the triton has an initial energy greater than that of the α-particle, the triton actually has a lower stopping power in GaN, due to its smaller mass. Thus, in the 1.6 µm depletion layer, the α-particle deposits 771 keV, while the triton deposits only 135 keV (Figure 39). By identifying the lower energy peak in the uncovered detector as the 135 keV triton peak, and the higher energy peak as the 771 keV α-particle, spectra from both detectors were energy calibrated.

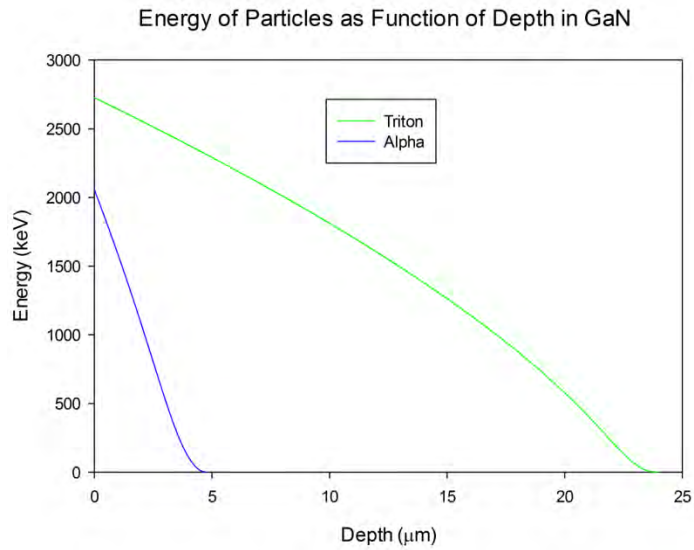

Figure 39. Residual energy of 2727 keV triton and 2055 keV α-particle as a function of surface depth in GaN.

Analysis of direct neutron detection in the covered detector was performed by comparing the acquired spectra to a Geant4 simulation of an identical GaN detector, 1 mm in diameter and 1.6 µm thick in a larger bulk GaN wafer (Figure 40). In the simulation, charged particles of ^{14}C and ^{1}H were simultaneously emitted in opposite directions, uniformly throughout the bulk GaN wafer. Energy deposited by either charged particle in the detector region was tallied to generate pulse height spectra, and then normalized to one source particle. The reaction rate was determined by calculating the neutron attenuation in the GaN detector:

$$(1 - e^{-\Sigma_c t})$$

where Σ_c is the macroscopic thermal capture cross section for GaN, and t is the detector thickness (1.6 µm). Results of the simulation were broadened using a 20 keV full-width half max (FWHM) Gaussian filter to approximate broadening in the actual detector. By examining the Geant4 spectra, a peak appears at 626 keV, which corresponds to the complete capture of both the ^{14}C and ^{1}H charged particles. The lower energy peaks are due to the convolution between each charged particles' stopping power and the thin depletion region in the detector. On the basis of specific spectral features in the simulation and experiment, it is hard to attribute the response of the covered detector to intrinsic neutron detection. This is primarily due to the low count rate in the detector, as a result of the small ^{14}N cross section. However, there is evidence of a double capture peak in the experimental spectra around 626 keV, indicating that the covered detector did respond intrinsically to thermal neutrons.

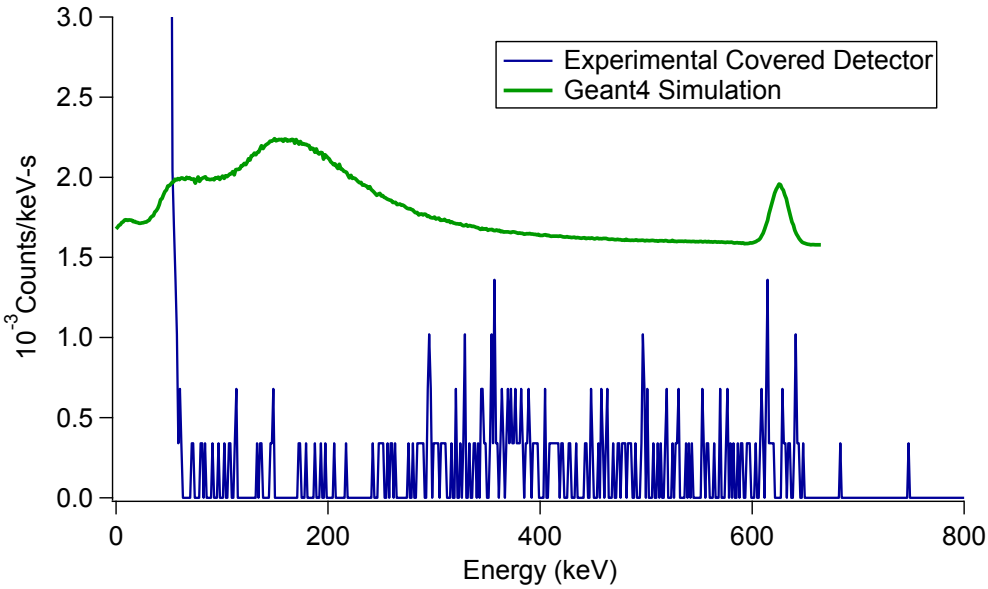

Figure 40. Spectra observed in covered detector and Geant4 simulated spectra. Geatn4 spectra is offset for clarity.

A stronger indication of intrinsic neutron detection is achieved when comparing the detection efficiency of the covered detector to the Geant4 simulation. By summing all counts in the experimental spectra above the low energy noise (> 50 keV) and dividing by the total neutron fluence presented to the detector, a detection efficiency of $(2.35 \pm 0.17) \times 10^{-4}$ % is found. Performing a similar analysis for the Geant4 simulation, a detection efficiency of $(2.93 \pm 0.59) \times 10^{-4}$ % is determined. Comparing the two, we see that the experimental efficiency falls within the uncertainty of the theoretical detection efficiency. This result, in addition to the appearance of a 626 keV double capture peak, and the inability to detect γ-rays in previous experiments, lends credibility to the conclusion that neutron capture is the source of the spectra, and not the presence of γ-rays in the neutron beam. We believe this result gives credence to the use of a partially depleted GaN detector for neutron detection with gamma discrimination.

4.2 Neutron Detection after In-core Irradiation

Our fabricated GaN devices were irradiated in the OSURR and their performance, for example, I-V, C-V, CCE, and alpha spectrum were tested before and after neutron irradiation.

The forward- and reverse-bias semi-log I-V characteristics of the GaN Schottky diodes at room temperature before and after neutron irradiation are shown in Figure 41. For the detector irradiated at 1×10^{15} n/cm^2, the current for forward bias and revers bias up to 4 V is nearly identical, whereas the irradiated device presents a slightly increase of reverse leakage current than that of the unirradiated one between -4 to -14 V. This phenomenon is consistent with a decrease of free carrier density, indicating increased defects density that increases hopping and/or tunneling transport through the diode. Similar behavior has been reported in neutron-irradiated GaN detectors by Grant [8,9]. There is a slight decrease of the forward current starting at approximately 1 V, which shows the trends to decrease rapidly when increasing the forward voltage. This indicates an increase in the GaN resistance for neutron irradiations greater than 10^{15} n/cm^2, as a result of creation the deep level traps. It is noteworthy that the loss of Schottky contact behavior is observed after $\approx 10^{16}$ n/cm^2 neutron irradiation for one of the devices (Figure 41). This is likely caused by interdiffusion at the metal-semiconductor interface, which can be enhanced by neutron irradiation (radiation-enhanced diffusion (RED)) [10]

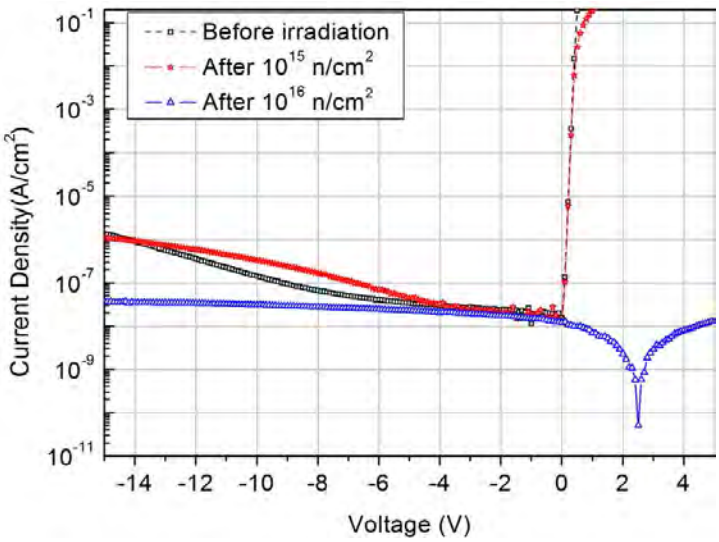

Figure 41. Forward- and reverse-bias I-V characteristics of a GaN radiation detector at room temperature before and after neutron irradiation at two neutron fluences.

Figure 42 presents the C-V measurements after neutron irradiation and compares them to measurements for the unirradiated detector. Results indicate the capacitance for a given reverse bias was reduced after the 10^{15} n/cm^2 fluence. This decrease is primarily caused by the deep levels induced by neutron irradiation. The effective carrier concentration was estimated (Figure 43) from the C-V data, giving values reasonable and consistent with those determined in previous studies [11,12]. Neutron-induced deep traps can cause carrier removal and compensation, leading to a decrease in carrier concentration. It has been reported that the formation of a disordered region in neutron-irradiated n-GaN can also

cause carrier removal [13].

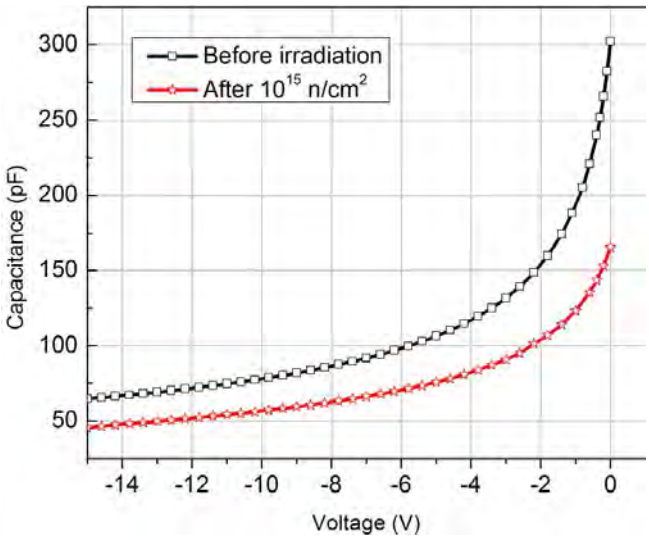

Figure 42. C-V measurements for a GaN radiation detector at room temperature before and after neutron irradiation (in two weeks).

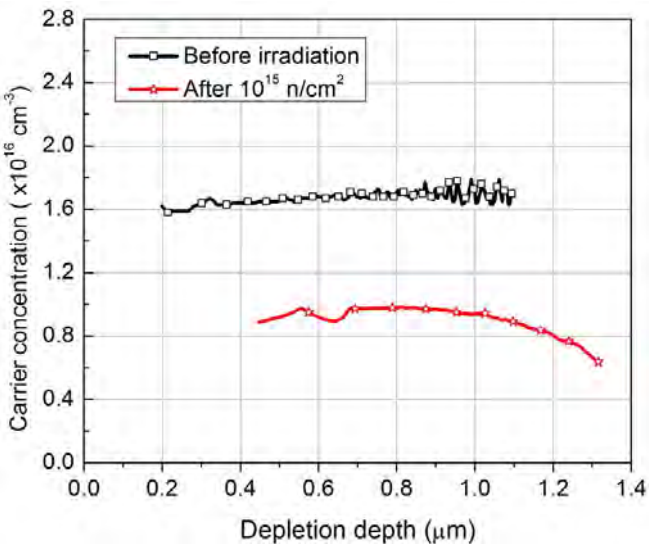

Figure 43. Concentration profiles derived from C-V measurements before and after neutron irradiation.

C-V measurements on the pre-irradiated device and 10^{15} n/cm^2 device indicated the depletion depth to be 0.97 µm and 1.32 µm, respectively, at a 15 V bias. It is known that the interface state at the interfacial layer between the semiconductor and the metal of the Schottky contact plays an important role in the I-V characteristics of the device [14]. Fast neutron collisions with weak bonds in this location can introduce new interface states, forming new energy levels and changing the interface state density. A consequence of this may explain the increased Schottky barrier height from 1.04 V to 1.68 V, as calculated from C-V data.

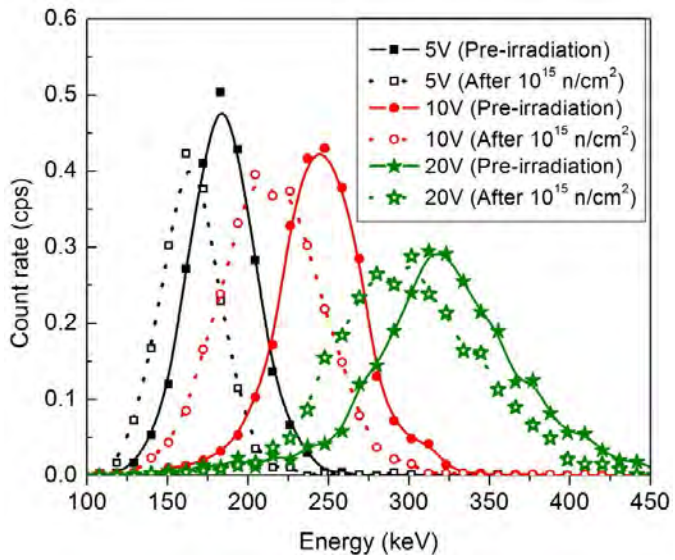

Figure 44. Alpha particle spectra measured using a ^{241}Am source at various reverse bias before and after neutron irradiation.

The spectroscopic response of the GaN detector to 5.48 MeV alpha particles from ^{241}Am before and after 10^{15} n/cm^2 fluence as a function of the applied voltage is shown in Figure 44. The spectra retained a similar shape, but moved towards lower energies. This lower-energy shift is caused by irradiation-induced electron trapped in the depletion region, which captures radiation-generated free carriers, resulting in reduced charge collection. While the C-V curve shows a increased depletion depth due to free carrel removal from irradiation, it does not necessarily refer that the more deposition of energy will produce more collected charge. The available charge to contribute to the pulse height is indeed reduced, resulting a red shifted energy spectrum, because of the capture and recombination of radiation induced electrons with deep traps.

The total gamma spectrum characterization of the irradiated GaN detector was performed two weeks after neutron irradiation, when the total radiation level of the devices has dropped to <2 µCi. The major activated radionuclides are ^{198}Au, ^{110m}Ag, and ^{60}Co, with half-lives of 2.7 d, 249.8 d, and 5.3 y, respectively. The three main characterizing gamma rays, with energies of 411 keV from 198Au, 657 keV from ^{110m}Ag, and 1173/1332 keV from ^{60}Co, are clearly identified in the gamma spectra in Figure 45, which was taken by an HpGe detector six days and two weeks after irradiation. While ^{198}Au originates in the Au metal deposited as contacts in the sensor itself and in the wire bindings, ^{110m}Ag originates in the Ag paste used to glue the GaN wafer to the DIP, and ^{60}Co originates in the DIP leads that are 29% nickel, 17% cobalt, and 54% iron. The residual radioactivity from the ^{110m}Ag and ^{60}Co can be easily eliminated if only the GaN wafer were irradiated. The downside of this evaluation method is the increased cost, because GaN must be reattached to the DIP to perform post-irradiation evaluation.

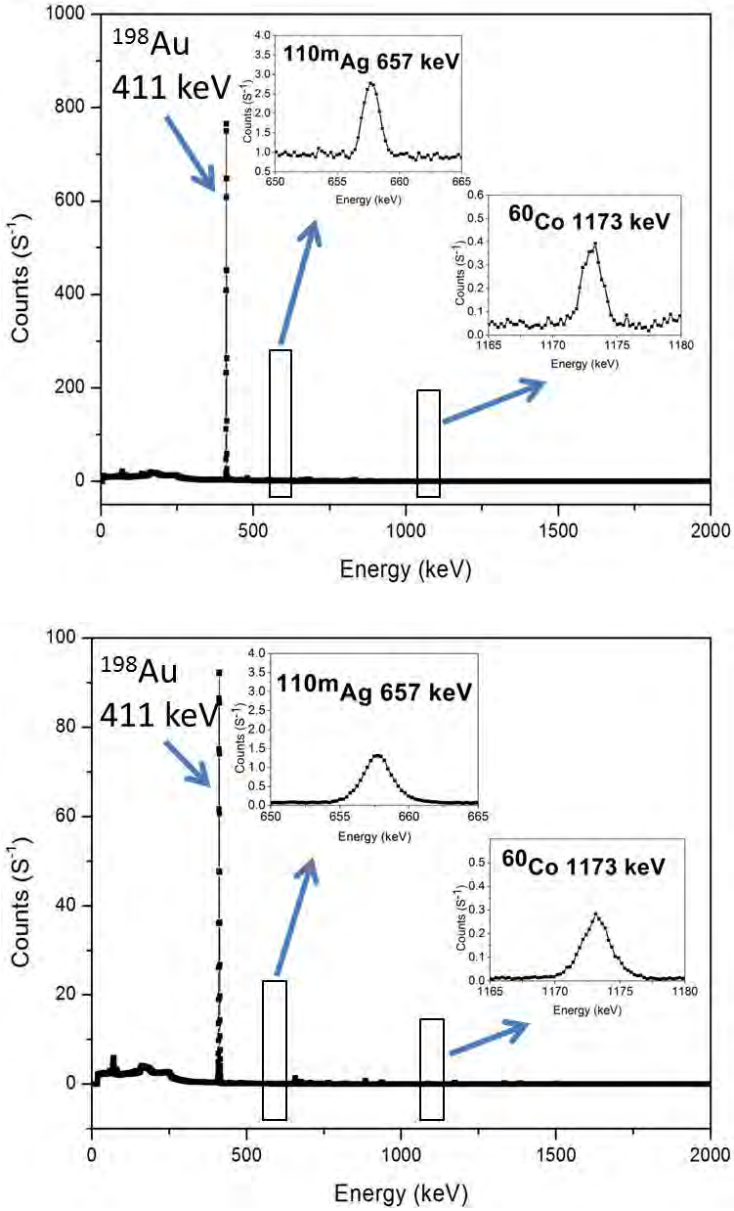

Figure 45. Gamma spectra of irradiated GaN device. Counts taken six days (above) and two weeks (below) after irradiation.

5. Conclusions

Neutron sensor based on GaN have been successfully fabricated and evaluated for their electronic performance and radiation response. Devices produced neutron signal in a high flux neutron beam at the OSURR. A switch from Ni/Au contacts to Pt contacts has lowered the leakage current in the detectors to below 1 nA at -20 V, and is more suitable for high temperature use, due to the high melting point of Pt. Devices have no response to gamma ray, demonstrated a good gamma discrimination capability. In-core irradiations of both GaN materials and devices have been performed at OSURR, and the off-line evaluation showed that sensors were only slightly degraded at 10^{15} cm^{-2} fluence. All major objectives have been accomplished except for a minor one, the sensor testing at high temperature. A heated testing chamber was fabricated for this testing at the beam line facility at OSURR. However, an unidentified electronic noise from ambient environment prevented the sensor from producing a meaningful neutron induced signal. The high temperature response of the sensor was still modeled with thermionic emission, which agrees well to an ex-situ experimental testing of sensors at 200 °C. The devices are expected to perform well at up to 800 °C, corroborated by SiC's alpha response at the same temperature. Simulations of our detectors using Sentaurus TCAD were also completed to provide fundamental understanding of device electronic properties. Finally, ten publications were produced from this work and one PhD and one Master student were graduated from working on projects related to this work.

6. Publication list

Journal Papers:

1) J.H. Wang, P. Mulligan, L. R. Cao, Transient Current Analysis of a GaN Radiation Detector by TCAD. *Nuclear Instruments and Methods in Physics Research Section A*:. Vol. 761, no. 11: 7-12. 2014.
2) Padhraic Mulligan, Jie Qiu, Jinghui Wang, Lei R. Cao, Study of GaN Radiation Sensor after In-core Neutron Irradiation. *IEEE Transaction on Nuclear Science*. Vol. 61, no. 4: 2040 - 2044. 2014
3) Evan. J. Katz, Chung-Han Lin, Jie Qiu, Zhichun Zhang, Umesh K. Mishra, Lei Cao, Leonard J. Brillson, Neutron Irradiation Effects on Metal-Gallium Nitride Contacts, *Journal of Applied Physics*, 115, 123705, 2014.
4) Chung-Han Lin, Evan J. Katz, Jie Qiu, Zhichun Zhang, Umesh K. Mishra, Lei Cao and Leonard J. Brillson, Neutron irradiation effects on gallium nitride-based Schottky diodes. *Applied Physics Letters*, Vol. 103, no. 16: 1-9. 2013.
5) Jie Qiu, Evan Katz, Chung-Han Lin, Lei Cao, Leonard J. Brillson, The Effect of Neutron Irradiation on Semi-insulating GaN. *Radiation Effects and Defects in Solids*. Vol. 168, 1- 9. 2013.
6) P. Mulligan, J.H. Wang, L. R. Cao, Evaluation of Freestanding GaN as an Alpha and Neutron Detector". *Nuclear Instruments and Methods in Physics Research Section A*:. Vol. 719, 13-16. 2013.
7) P. Mulligan, J.H. Wang, L. R. Cao, Study of GaN for Neutron Detection in High Flux Environment, *IEEE Transaction on Nuclear Science*. (submitted)

Conference Proceedings

8) Jinghui Wang, Padhraic L. Mulligan, and Lei R. Cao. TCAD Simulation of Charge Collection in GaN Schottky Diode Radiation Detector. *American Nuclear Society 2014 Annual Meeting*. Vol. 110. (2014): 167 - 169.
9) Padhraic L. Mulligan, Jinghui Wang, and Lei R. Cao. Developing a Radiation Detector on Freestanding n-GaN. *American Nuclear Society 2013 Annual Meeting*. Vol. 108. (2013): 253 - 254.
10) Jie Qiu, Evan Katz, Lei R. Cao, Leonard J. Brillson. The Evaluation of GaN for Neutron Detector with Cathodoluminescence Spectroscopy. *American Nuclear Society 2012 Winter Meeting*. Vol. 107. (2012): 357 - 359.

7. References

1. Ganchenkova, M.G. and R.M. Nieminen, *Nitrogen vacancies as major point defects in gallium nitride.* Physical Review Letters, 2006. 96(19).

2. Griesmann, U., *GDS II Toolbox ver. 114a*, 2014.

3. Zhaojun, L., et al., *Thermal stability of Schottky contacts on strained AlGaN/GaN heterostructures.* Applied Physics Letters, 2004. 84(9): p. 1585-1587.

4. Lu, W., et al., *A comparative study of surface passivation on AlGaN/GaN HEMTs.* SSE</cja:jid> Solid State Electronics, 2002. 46(9): p. 1441-1444.

5. Cheung, S.K. and N.W. Cheung, *Extraction of Schottky diode parameters from forward current-voltage characteristics.* Applied Physics Letters, 1986. 49(2): p. 85.

6. Ziegler, J.F., M.D. Ziegler, and J.P. Biersack, *SRIM - The stopping and range of ions in matter (2010).* Nuclear Instruments and Methods B, 2010(268): p. 1818.

7. Nemirovsky, Y., et al., *Study of the Charge Collection Efficiency of CdZnTe Radiation* Detectors. Journal of Electronic Materials, 1996. 25(8): p. 1221.

8. Grant, J., et al., GaN as a radiation hard particle detector. Nuclear Instruments and Methods in Physics Research Section A: Accelerators, Spectrometers, Detectors and Associated Equipment, 2007. 576(1): p. 60-65.

9. Chung-Han Lin, Evan. J. Katz, Jie Qiu, Zhichun Zhang, Umesh K. Mishra, Lei Cao, and Leonard J. Brillson, *Neutron Irridiation Effects on Gallium Nitrode-Based Schottky Diodes*. Applied Physics Letter, 2013(103): p.162106.

10. G. J. Dienes and A. C. Damask, *Radiation enhanced diffusion in solids*. Journal of Applied Physics, 1958(29): p. 1713.

11. A. Owens, A. Barnes, R.A. Farley, M. Germain, and P.J. Sellin, *GaN detector development for particle and X-ray detection*, Nuclear Instruments and Methods in Physics Research Section A: Accelerators, Spectrometers, Detectors and Associated Equipment, 2012(695): p.303.

12. S. Nakamura, *GaN growth using GaN buffer layer*, Journal of Applied Physics, 1991(30) p. L1705.

13. A. Y. Polyakov, S. J. Pearton, P. Frenzer, F. Ren, L. Liu, and J. Kim, Radiation effects in GaN materials and devices, Journal of Material Chemistry C, 2013(a): p. 877.

14. H. H. Tseng and C. Y. Wu, *A simple interfacial-layer model for the nonideal I-V and C-V characteristics of the Schottky-barrier diode*, Solid-State Electronics, 1987(30): p. 383.